Journal of South American Earth Sciences 90 (2019) 54–69

Contents lists available at ScienceDirect

Journal of South American Earth Sciences

journal homepage: www.elsevier.com/locate/jsames

Isotopic and geochemical characterization of the metavolcano-sedimentary rocks of the Jirau do Ponciano Dome: A structural window to a Paleoproterozoic continental arc root within the Southern Borborema Province, Northeast Brazil

Haroldo M. Lima[a,*], Márcio M. Pimentel[b,1], Lauro Cézar M. de Lira Santos[c], Elton L. Dantas[b]

[a] Universidade Federal do Ceará, Campus do Pici, 912, CEP 60440-554, Fortaleza, Ceará, Brazil
[b] Programa de Pós-graduação em Geologia, Universidade de Brasília, Campus Universitário Darcy Ribeiro ICC, Asa Central, CEP 70919-970, Brasília, DF, Brazil
[c] Universidade Federal de Pernambuco, Departamento de Geologia, Av. da Arquitetura, Cidade Universitária, CEP 50740-540, Recife, PE, Brazil

ARTICLE INFO

Keywords:
Jirau do Ponciano Dome
Sergipano fold belt
Southern Borborema province

ABSTRACT

The Sergipano Fold Belt is a Neoproterozoic orogen exposed in the southern Borborema Province (Northeast Brazil), which is interpreted as the result of the oblique convergence process between the São Francisco-Congo block and smaller crustal fragments. The Nicolau-Campo Grande Complex is the metavolcanic-sedimentary portion of the Jirau do Ponciano Dome, an important basement inlier within this collisional belt. Whole-rock-geochemical major and trace-element data of major and trace elements from the metavolcanic rocks of the Nicolau-Campo Grande Complex indicate basaltic-andesite, andesitic, rhyodacitic, and rhyolitic compositions. Rare earth element and trace elements show the typical signature of magmatic arc rocks with negative Nb, Ta, P, and Ti anomalies. New U-Pb zircon data from amphibolite and hornblende-biotite paragneiss samples from the complex confirm the existence of a Paleoproterozoic zircon population of a Paleoproterozoic age of approximately ca. 2054 Ma with Archean inheritance ranging in age between 2779 and 3324 Ma. A maximum sedimentation age of 2028 Ma is constrained by the youngest zircon grain in the hornblende-biotite paragneiss. Zircon U-Pb data from the metarhyolite and rhyodacites indicate Paleoproterozoic ages of ca. 2061 and 2074 Ma, respectively, interpreted as their crystallization age. Nd isotopic data in the metarhyolite and rhyodacites indicate Nd T_{DM} ages between 2.54 and 3.07 Ga and $^{87}Sr/^{86}Sr$ $(_{2061Ma})$ values from 0.71396 to 0.72351. Based on these data, we suggest that the probable source area of the metavolcanic-sedimentary complex is a Paleoproterozoic magmatic arc that was exhumed and covered by the paleobasins of the Macururé Domain in the northeast portion of the Sergipano Fold Belt.

1. Introduction

The understanding of the formation and significance of gneissic-migmatitic domes is a prerequisite to investigate the roots of continental arcs as well as crust melting processes during convergent plate motions (Burg et al., 2004). Collisional tectonics are characterized by intense crustal growth and reworking in response to deformation, metamorphism, and magmatism (Whitney et al., 2004) followed by crustal exhumation that might expose ancient high-grade rocks from the middle-lower crust through structural windows, such as dome structures (Yin, 2004). In the southern Borborema Province (BP), Northeast Brazil, metavolcanic-sedimentary sequences are grouped in the Sergipano Fold Belt, which consists of a Brasiliano/Pan-African collisional orogen that resulted from the oblique convergence between the São Francisco Craton and smaller crustal fragments (Oliveira et al., 2010; Lima et al., 2018).

Basement rocks within the belt are exposed in the Jirau do Ponciano, Itabaiana, and Simão Dias domes, which are partially covered by supracrustal rocks (Amorim, 1995; D'el Rey Silva and McClay, 1995; D'el Rey Silva, 1999; Oliveira et al., 2015). The Jirau do Ponciano Dome (JPD) represents an inverted anticline and consists mainly of tonalite to granodiorite high-grade orthogneisses interleaved with metavolcanic-sedimentary rocks of the Nicolau-Campo Grande Complex (NCCG; Brito and Mendes, 2011, Fig. 1a). This dome is confined by

* Corresponding author.
E-mail addresses: haroldogeo@ufc.br (H.M. Lima), lauromontefalco@gmail.com (L.C.M. de Lira Santos).
[1] In Memorian.

https://doi.org/10.1016/j.jsames.2018.12.002
Received 27 June 2018; Received in revised form 30 November 2018; Accepted 1 December 2018
Available online 04 December 2018

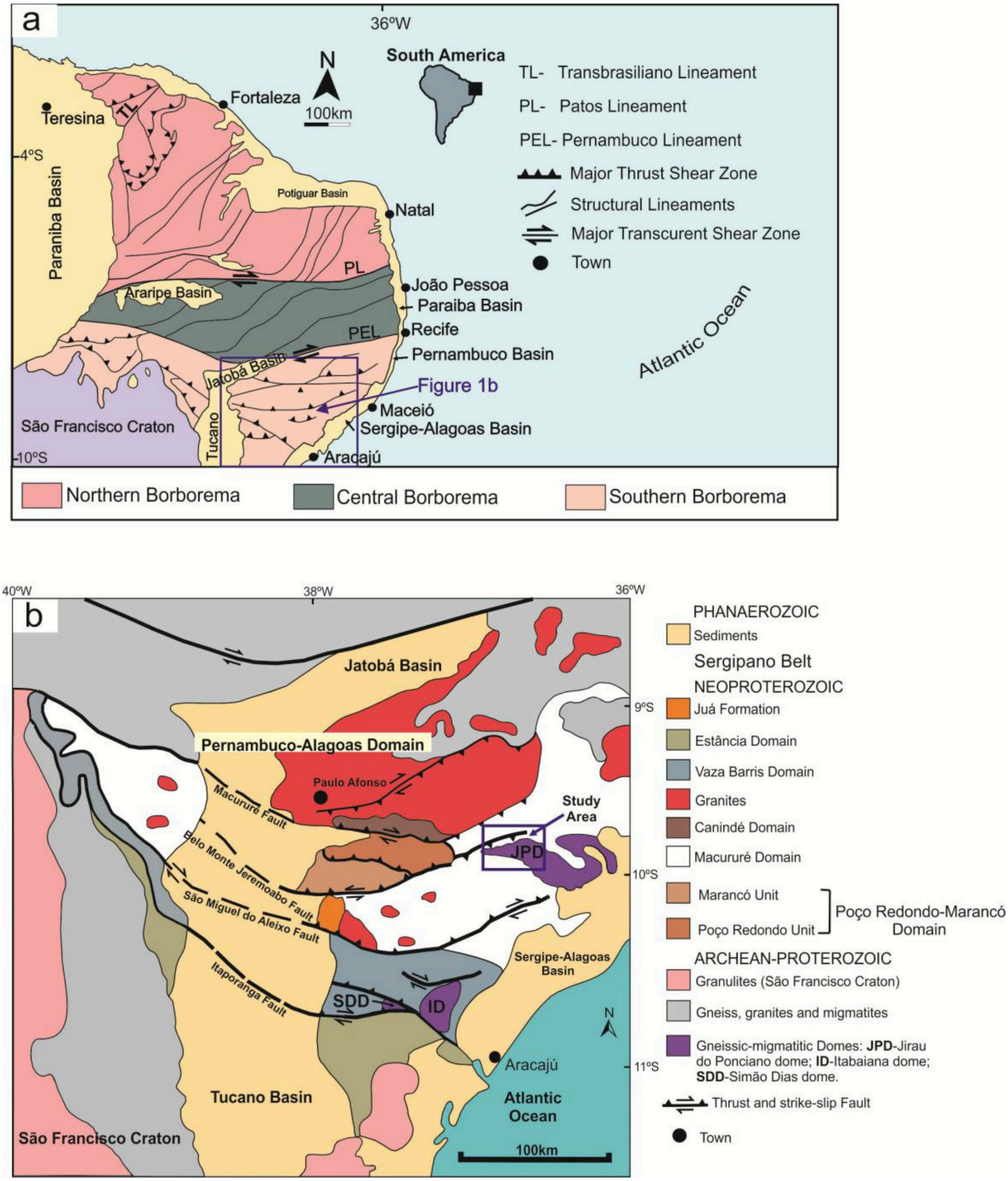

Fig. 1. a) Schematic map of Borborema Province showing the three sub-provinces with emphasis on the Sergipano Fold Belt (modified from Brito Neves et al., 2000). b) Map of the Sergipano Fold Belt showing the main Paleoproterozoic gneiss domes (modified from D'el-Rey Silva, 1999; Oliveira et al., 2010, 2015).

thrust faults that are interpreted as being responsible for its uplift and exposure. Supracrustal rocks of the NCGC consist of metapelitic to metapsammitic rocks as well as felsic, intermediate, and mafic metavolcanic members.

The genetic relationship between this and other domes of the Sergipano Fold Belt, which also host supracrustal sequences, as well as their significance to the BP origin remain poorly understood, except for studies at a very regional scale (e.g., D'el Rey Silva, 1999; Oliveira et al., 2010, 2015). In this work, whole rock geochemical, Nd-Sr isotopic, and U-Pb geochronologic data are presented for the NCGC metavolcanic rocks. The provenance of the metasedimentary rocks of this sequence is also discussed. The results include clues on the nature, age, and tectonic setting of pre-Borborema crustal evolution as well as insights on the nature of the basement domains of Western Gondwana, as the supracrustal sequences associated with the gneissic domes represent unique structural window exposures to investigate the early crust of the Neoproterozoic mobile belts. Lastly, the definitions of NGCC geochemical and geochronological parameters are compared to other abundant Transamazonian-Eburnean (2.0–2.2 Ga) supracrustal sequences of Northeast Brazil and West Africa to contribute to our knowledge of the Gondwana basement evolution.

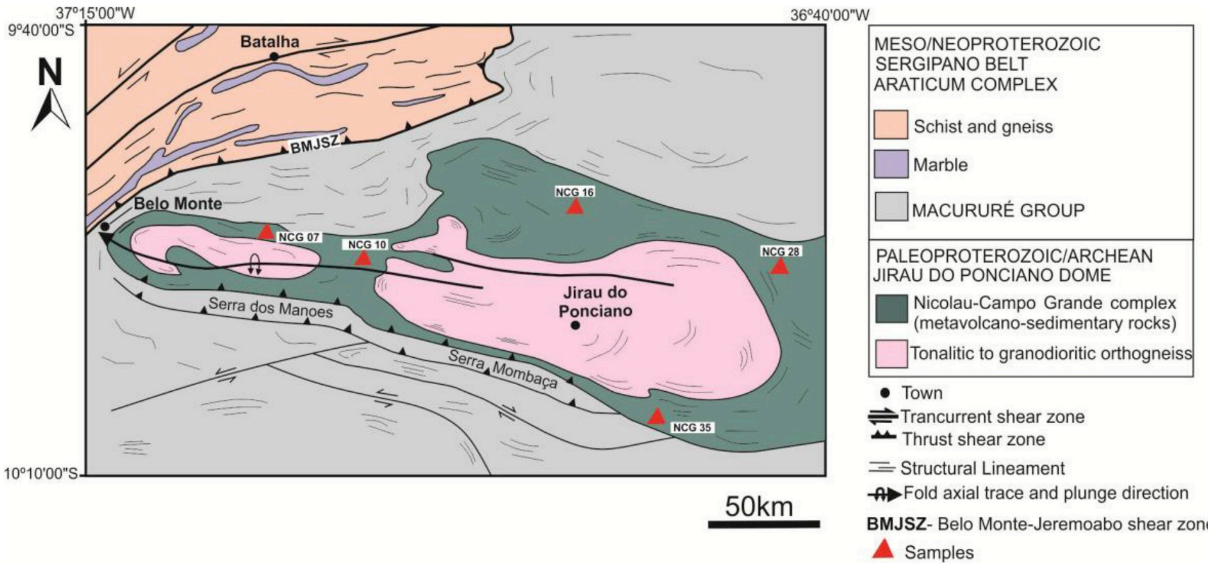

Fig. 2. Simplified geological map of the Jirau do Ponciano Dome displaying the Nicolau-Campo Grande Complex and location of zircon U-Pb Geochronology samples.

2. Geological setting

The BP represents a complex Neoproterozoic orogenic system characterized by crustal rocks of the Archean-Paleoproterozoic basement, covered by Meso-to Neoproterozoic sequences that are largely intruded by numerous granitic plutons (Almeida et al., 1981; Brito Neves et al., 2000, 2014). Its tectonic framework is interpreted to be a result of a crustal collage that formed during the assembly of Western Gondwana during the early to late Neoproterozoic (Brito Neves et al., 1995; Santos, 1995; Santos et al., 2010, 2017, 2018). Intracontinental inverted rifts that occurred at ca. 640–630 Ma are also a possible interpretation for BP evolution (Neves et al., 2015). The province comprises three sub-provinces bounded by the Patos and Pernambuco lineaments: northern, central, and southern (Van Schmus et al., 1995, 2011; Brito Neves et al., 2014; see Fig. 1a).

In the southern sub-province, the Sergipano Fold Belt is interpreted as a Brasiliano/Pan-African collisional orogen, formed by the oblique collision of the São Francisco Craton and the Pernambuco-Alagoas Domain (D'el Rey Silva, 1999; Oliveira et al., 2010; Lima et al., 2017; see Fig. 1b). Nevertheless, the crustal boundary between the Sergipano Fold Belt and the Pernambuco-Alagoas domain remains unclear. The Sergipano Fold Belt includes five lithotectonic domains from south to north as follows: Estância, Vaza-Barris, Macururé, Marancó-Poço Redondo, and Canindé (Oliveira et al., 2006, Fig. 1b). They are composed of Neoproterozoic metavolcanic and metasedimentary sequences; granitic intrusions; and three major exposed gneiss-migmatite domes: Simão Dias and Itabaiana in the Vaza Barris Domain and Jirau do Ponciano in the Macururé Domain (Santos et al., 1998; D'el Rey Silva, 1999, Fig. 1b).

The Simão Dias and Itabaiana domes are interpreted as uplifts of the São Francisco Craton basement to the north (D'el-Rey Silva and McClay, 1995; Oliveira et al., 2015; Lima et al., 2018). However, the tectonic link between the craton and the Jirau do Ponciano Dome (JPD) has not yet been proven and its significance for the Southern BP evolution remains unknown.

Local structural studies suggest that rocks from Jirau do Ponciano Dome form a large-scale anticline with an E-W axis, slightly inflecting to the NW-SE with the axial surface dipping to the S/SW (Brito and Mendes, 2011). The dome has an elliptical form, outcropping within the Neoproterozoic Macururé Domain. Isotope data from the dome is scarce and inconclusive. Early geochronological determinations obtained by the Rb-Sr method for the orthogneisses of the JPD suggest a 2500-Ma crystallization age of the rock protolith (Amorim et al., 1993). Such studies suggest that the major gneisses corresponds to a typical TTG association, corresponding to part of the basement of the Sergipano Fold Belt.

The dome is mainly composed of gray orthogneisses with granitic, granodioritic, and tonalitic protolith compositions. In addition, these rocks show a variety of migmatitic structures on well-developed metatexites, including stromatic to strongly folded fabrics. Such rocks compose the major core, which is surrounded and partially covered by the NCGC supracrustal rocks that form slightly to highly deformed metapelitic and metapsammitic members as well as metavolcanic lithotypes, the main focus of this study (Fig. 2).

3. Field aspects

The NCGC consists of metasedimentary members dominated by hornblende-biotite paragneisses, biotite schists, biotite-chlorite schists, quartzites, and minor biotitites in addition to metavolcanic rocks represented by metarhyolites-rhyodacites and amphibolites. These rocks cross-cut and surround tonalitic and granodioritic gneisses of the JPD. Elongated xenoliths of these metaplutonic rocks may occur in deformed volcanoclastic rocks of the NCGC, indicating that they must be older than the rocks from the studied supracrustal sequence.

The hornblende-biotite paragneisses are medium-to fine-grained and show discrete banding, alternating between mafic bands consisting of hornblende and biotite and quartz-feldspar felsic bands or even showing mylonitic structure (Fig. 3a and b). The biotite-chlorite schists occur as interleaved lenses in the hornblende-biotite paragneisses and are intensely deformed and weathered showing centimetric plagioclase segregations (Fig. 3c).

Quartzite subordinately occurs, forming metric lenses interleaved with biotite-chlorite schists. These rocks show some hematite concentrations, whereas biotites are restricted and associated with local low-angle shear zones resulting from an anomalous concentration of secondary biotite. Biotites might also be characterized by punctual occurrences of phlogopite lamellae, suggesting metasomatic processes in the region (Fig. 3d).

Metarhyolite and metarhyodacite members are leucocratic and occur as metric sheets, showing variable stages of ductile deformation. They show strong foliation near the low-angle shear zones (Fig. 3e), as well as slightly blue quartz phenocrysts in a fine-grained matrix of quartz, feldspar, and biotite. The amphibolites are mostly mesocratic, deformed, and weathered, occurring interleaved with schists and paragneisses (Fig. 3f). Their foliated structure is marked by the

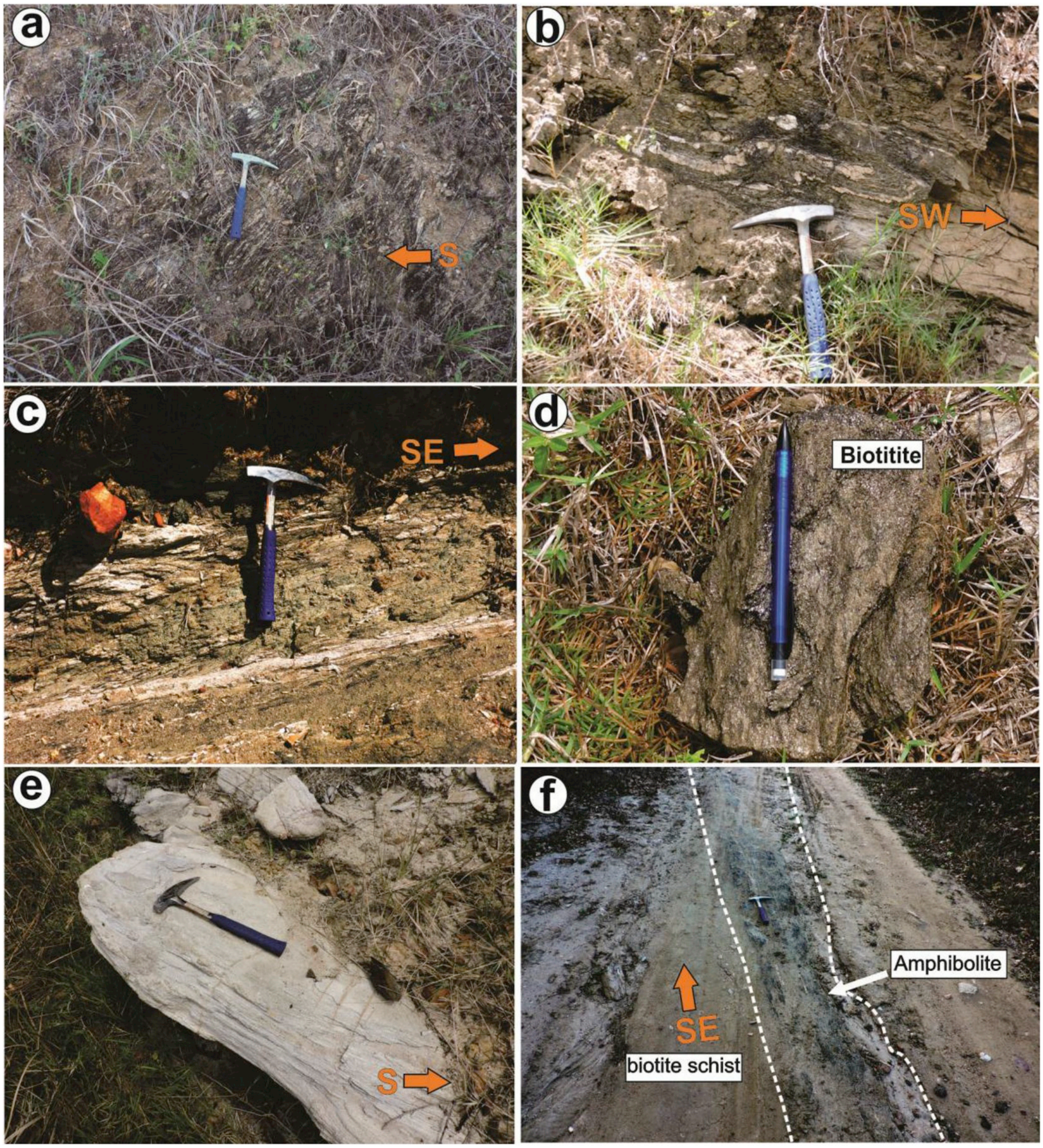

Fig. 3. Field features of the Nicolau-Campo Grande metavolcano-sedimentary complex: a) Banded hornblende-biotite paragneiss and deformed intensely in high-angle tectonics with southern dip b) Folded hornblende-biotite paragneiss with incipient migmatization in low-angle shear zone. c) Biotite-chlorite schist deformed in strike-slip shear zone. d) Biotitite. e) Metarhyodacite showing low-angle foliation dipping 35° to the south. f) Amphibolite lens interleaved in biotite schists.

orientation of amphiboles and segregation of plagioclase constituting centimetric felsic bands and minor venules with concentrations of biotite cross-cutting the main rock structure.

3.1. Petrography

3.1.1. Metasedimentary rocks

Samples of hornblende-biotite paragneisses show a medium-to fine-grained granoblastic texture, and consist of quartz (40%), potassium feldspar (5–20%), plagioclase (10–25%), hornblende (15–30%), biotite (20–25%), chlorite (2–10%), apatite (1–2%), sillimanite (1–5%), and minor zircon and opaque grains (1%). The quartz crystals show grain border migration-type recrystallization and undulating extinction and form 0.5–2-mm ribbons oriented along the foliation. Subhedral 1–3-mm-long hornblende crystals are commonly altered to biotite and chlorite. Plagioclase crystals are 1–2 mm in length and show deformation and undulose extinction. Potassium feldspar is represented by microcline and occurs as 2–5-mm-long rotated porphyroclasts. Subhedral biotite lamellae with opaque inclusions are oriented along the regional foliation and rarely show equilibrium texture with the amphibole.

Biotite schists and biotite-chlorite schists correspond to the medium-grained rocks, showing a lepidoblastic texture, and are composed of quartz (40–55%), plagioclase (40–50%), chlorite (20–25%), biotite (30%), sillimanite (5%), and accessory minerals such as zircon and opaque minerals (1%) and to lesser extent garnet, muscovite, apatite, and monazite (< 5%). In these rocks, probable hydrothermal alteration led to the formation of plagioclase and biotite venules cutting through the schistosity (Fig. 4a). The biotitization process is confirmed by the presence of secondary biotite comprising more than 95% of the rock (Fig. 4b). Quartzite shows modal composition including quartz (95%) and muscovite (5–10%). Some samples contain up to 2% hematite.

3.1.2. Metavolcanic rocks

The metarhyolites and metarhyodacites are composed of anhedral quartz (35–40%), subhedral to anhedral (25–40%) plagioclase, subhedral to anhedral potassium feldspar (30–40%), subhedral biotite (1%), and anhedral chlorite (1%). Opaque minerals and sericite are

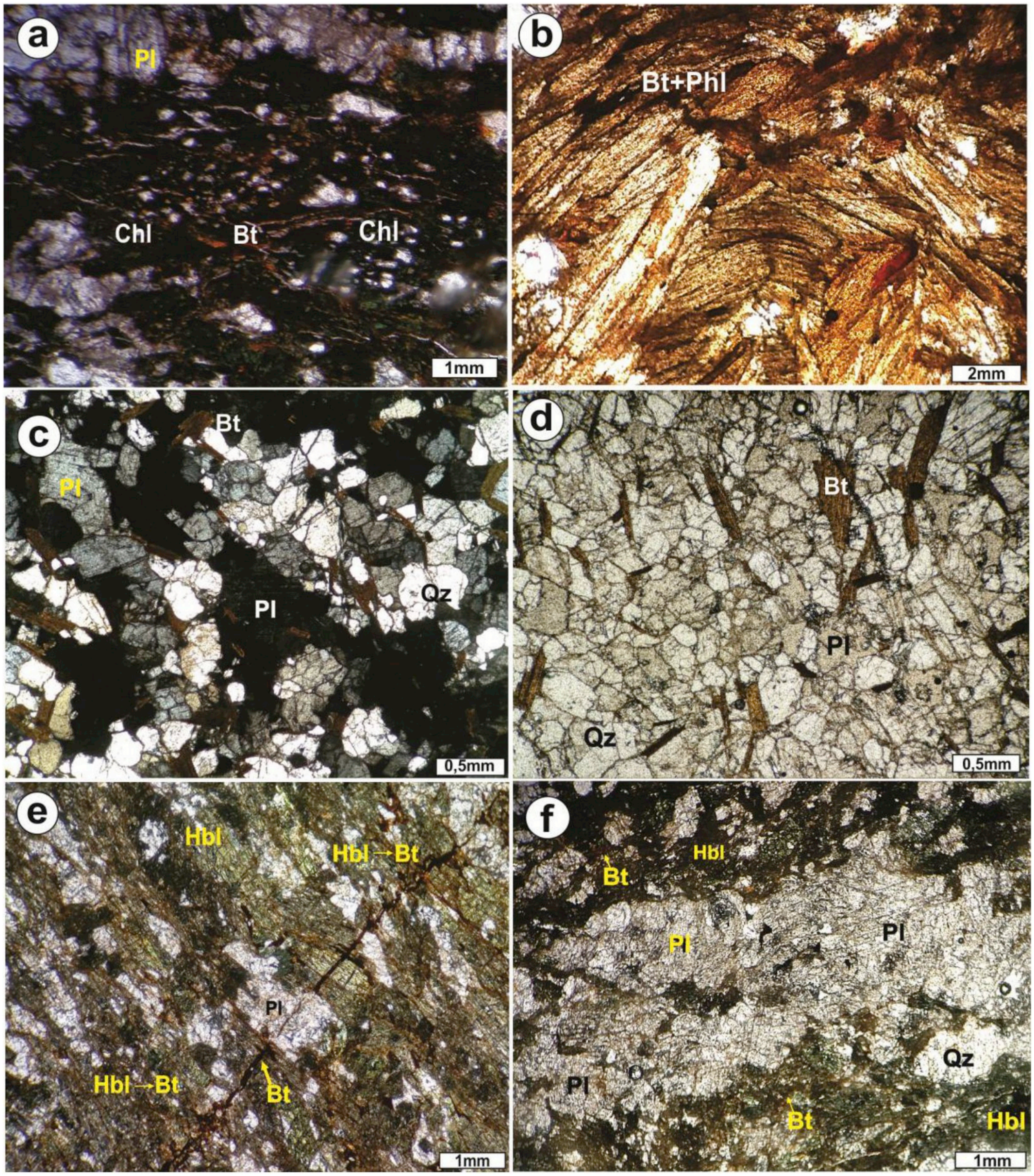

Fig. 4. Mineralogical features and textures of metavolcanic and metasedimentary rocks: a) Biotite-chlorite schist showing plagioclase and chlorite crystals. b) Biotitite with ductile deformation of biotite and some opaque minerals. c) Metarhyolite with inequigranular, granoblastic texture and dominant plagioclase and quartz. d) Metarhyolite exhibiting subhedral to euhedral biotite in quartz-feldspar matrix. e) Amphibolite texture with venules of biotitization cutting hornblende and plagioclase. f) Banded amphibolite with alteration of hornblende to biotite. Qz-quartz, Bt-biotite, Pl-plagioclase, Hbl-hornblende, Chl-chlorite, Phl-phlogopite.

Table 1
Composition of major elements (wt %) in intermediate to acidic metavolcanic rocks and amphibolites from Nicolau-Campo Grande Complex (NCGC).

Sample	Metarhyolite-metarhyodacites								Amphibolite (basaltic andesite and andesite)									
	NCG16	NCG17	NCG18	NCG19	NCG20	NCG21	NCG22	NCG28	NCG3	NCG4	NCG5	NCG6	NCG7	NCG8	NCG9	NCG10	NCG11	NCG12
SiO_2	74.6	76.1	75.2	76.1	75.6	73.7	74.9	74.7	53.4	54.2	57.7	50.4	51.5	51.4	53	53.5	51.8	51.2
TiO_2	0.17	0.13	0.15	0.12	0.17	0.14	0.14	0.16	0.8	0.79	0.79	0.99	0.98	0.92	1.01	0.97	0.92	0.92
Al_2O_3	14.5	14.1	14.8	14.15	14.8	14.1	13.55	14.7	13.8	13.15	12.95	13.4	13.7	13.7	13.85	14.05	13.65	13.65
Fe_2O_3(total)	1.41	1.15	1.15	1.11	1.4	1.2	1.13	1.19	11.85	11.4	11.35	13.15	13.4	13.2	13.1	12.95	12.6	13
MnO	0.01	0.01	0.01	0.01	0.01	0.01	0.01	0.02	0.12	0.12	0.12	0.15	0.15	0.15	0.13	0.13	0.13	0.14
MgO	0.43	0.34	0.28	0.32	0.43	0.26	0.26	0.29	4.77	4.94	4.9	5.7	5.85	5.73	5.81	5.75	5.6	5.69
CaO	2.11	2.03	2.01	2	2.13	1.93	1.83	1.99	6.5	6.73	6.69	8.06	8.23	7.83	8.42	8.06	7.78	7.62
Na_2O	4.9	4.48	5.07	4.47	5.02	4.86	4.67	5.06	2.6	2.66	2.64	2.36	2.43	2.47	2.58	2.68	2.63	2.52
K_2O	1.19	1.78	2.16	1.79	1.12	2.06	1.98	2.18	0.39	0.4	0.39	0.43	0.45	0.41	0.41	0.39	0.37	0.4
P_2O_5	N.d	N.d	0.17	N.d	N.d	0.19	0.18	0.17	0.04	0.08	0.06	0.09	0.1	0.1	0.1	0.11	0.11	0.09
LOI	0.92	0.8	0.58	0.89	0.93	0.47	0.52	0.54	3.72	3.93	3.66	3.42	3.41	3.31	3.12	3.17	3.18	3.35
Total	99.32	100.12	100.83	100.07	100.68	98.26	98.47	100.29	98	98.4	101.25	98.15	100.2	99.22	101.53	101.76	98.77	98.58

Table 2
Composition of trace and rare earths elements (ppm) of metavolcanic rocks from Nicolau-Campo Grande Complex (NCGC). N.d.-No detected. * REE normalized for the primitive mantle of McDonough and Sun (1995).

Sample	Metarhyolite-metarhyodacites								Amphibolite (basaltic andesite and andesite)									
	NCG16	NCG17	NCG18	NCG19	NCG20	NCG21	NCG22	NCG28	NCG3	NCG4	NCG5	NCG6	NCG7	NCG8	NCG9	NCG10	NCG11	NCG12
Sc	2	2	1	2	2	1	1	1	31	32	31	40	40	41	39	39	40	42
V	19	23	14	19	17	14	15	16	224	227	218	264	259	267	226	224	237	277
Cr	10	10	10	10	10	10	20	10	260	250	240	180	190	190	160	160	170	190
Co	28	38	21	37	28	33	32	21	42	43	42	48	46	48	56	54	55	51
Li	10	N.d	10	10	10	10	10	10	N.d	N.d	N.d	N.d	N.d	N.d	N.d	N.d	N.d	N.d
Mo	0.43	0.34	0.28	0.32	0.43	0.26	0.26	0.29	4.77	4.94	4.9	5.7	5.85	5.73	5.81	5.75	5.6	5.69
Ni	3	3	2	3	4	4	2	2	88	91	92	106	105	108	99	98	100	112
Cu	4	6	13	4	6	17	17	13	54	56	56	51	50	51	61	60	62	54
Zn	12	12	14	10	12	15	15	14	122	125	124	135	137	137	141	141	141	145
Ga	17.6	16.1	21.1	16	17.6	21	21.5	20.2	23.1	22.7	23.3	21.4	21.1	20.8	20.4	20.9	22	20.2
Rb	35.6	35.2	60.1	35	34.8	61.4	58.2	58.1	4.7	4.5	4.4	2.5	2.7	2.5	2.1	2.1	2.3	2.4
Sn	1	2	3	1	2	3	3	3	2	2	3	2	2	2	2	3	2	2
Sr	299	240	272	241	300	269	264	256	211	212	217	193.5	203	191.5	184.5	188	196	192
W	223	328	179	324	221	290	282	187	40	44	40	32	32	32	64	64	66	32
Zr	97	132	96	117	187	85	81	94	155	146	154	100	75	88	129	131	138	85
Nb	11.1	5.2	6.3	5.3	11.2	6.1	5.8	6	29.2	27.2	30.1	24.5	26.9	25,3	42,1	42,2	39,2	24,9
Cs	1,6	1,43	2,35	1,45	1,71	2,26	2	2,14	0,14	0,18	0,16	0,06	0,11	0,17	0,21	0,22	0,2	0,03
Ba	445	608	574	603	446	557	523	543	240	248	247	208	219	228	145,5	148	149	202
La	30.5	37.8	23.5	39.2	32.1	22.7	21.1	21.2	15.5	15.5	15.4	9.9	12	12	14.5	15.4	15.9	11.4
Ce	43.4	54.6	46.9	53.3	44.6	44.4	43.9	41.5	23.3	23.7	25.1	15.4	17.8	18.3	21.2	21.9	22.5	16.9
Pr	4.69	5.64	5.34	5.79	4.7	5.19	4.57	4.7	3.21	3.28	3.38	2.44	3	2.99	3.43	3.6	3.62	2.94
Nd	14.3	16.8	18.7	16.8	14.2	17.8	18.5	17.1	15.4	16	15.6	11.9	12.1	13.2	14.1	15.4	16.3	12.1
Sm	2.25	2.49	3.92	2.53	2.29	3.95	4.03	3.69	4.28	4.21	4.89	3.2	3.74	3.66	4.93	4.73	4.78	3.33
Eu	0.64	0.69	0.52	0.66	0.65	0.5	0.57	0.51	1.31	1.33	1.28	1.22	1.18	1.22	1.39	1.39	1.48	1.09
Gd	1.63	1.96	2.55	2.19	1.77	2.72	2.87	2.82	5.94	5.58	5.64	5	5.15	4.96	5.9	5.66	6.56	4.63
Tb	0.28	0.31	0.3	0.3	0.28	0.33	0.33	0.35	1.01	1.02	0.99	0.91	0.98	0.89	1.11	1.16	1.11	0.84
Dy	1.28	1.44	1.55	1.57	1.46	1.82	1.58	1.66	6.65	6.25	6.1	5.6	5.81	5.98	7.37	7.44	7.15	5.42
Ho	0.26	0.29	0.33	0.29	0.32	0.33	0.32	0.37	1.27	1.27	1.31	1.14	1.35	1.35	1.6	1.54	1.7	1.27
Er	0.64	0.76	0.91	0.79	0.77	0.91	1.01	1	3.85	3.84	3.83	3.31	3.73	3.9	4.37	4.39	4.66	3.58
Tm	0.13	0.1	0.14	0.11	0.14	0.16	0.2	0.13	0.57	0.55	0.54	0.48	0.56	0.54	0.61	0.67	0.64	0.49
Yb	0.6	0.7	0.96	0.67	0.84	1.08	0.79	0.83	3.54	3.4	3.53	3.19	3.45	3.49	4.22	4.13	4.24	3.35
Lu	0.1	0.12	0.13	0.1	0.13	0.17	0.16	0.19	0.5	0.45	0.45	0.47	0.53	0.52	0.54	0.6	0.62	0.45
Y	5.9	7.7	9.9	7.8	8	10	9.5	9.7	36.5	36	36.5	30.9	33.7	31.8	38.7	39.2	39.3	30.8
Hf	3	4.1	3.2	3.6	5.7	3	3.1	3.4	4.6	4.3	4.5	3.1	2.4	2.8	3.9	3.7	3.7	2.5
Ta	0.4	0.4	0.7	0.4	0.3	0.9	0.8	0.7	0.5	0.4	0.4	0.3	0.3	0.3	0.4	0.5	0.5	0.3
Pb	20	27	14	24	24	13	11	13	5	9	N.d	5	2	N.d	3	6	N.d	N.d
Th	8.95	17.55	12.65	17.65	8.97	12.1	13.3	11.7	1.06	1.04	1.01	0.59	0.59	0.54	0.64	0.67	0.73	0.51
U	0.48	0.77	2.42	0.76	0.92	2.38	2.51	2.2	0.2	0.19	0.18	0.16	0.16	0.18	0.23	0.24	0.26	0.11
ΣREE	100	123	105	124	104	102	99	96	86	86	88	64	71	73	85	88	91	67
Eu/Eu*	1.02	0.95	0.50	0.86	0.99	0.47	0.51	0.48	0.79	0.84	0.74	0.93	0.82	0.87	0.79	0.82	0.81	0.85
$(La/Yb)_N$	34.59	36.75	16.66	39.82	26.01	14.30	18.18	17.38	2.98	3.10	2.97	2.11	2.37	2.34	2.34	2.54	2.55	2.32
$(La/Sm)_N$	8.49	9.51	3.76	9.71	8.78	3.60	3.28	3.60	2.27	2.31	1.97	1.94	2.01	2.05	1.84	2.04	2.08	2.14

subordinate. Quartz crystals have dimensions of approximately 1–2 mm, with subgrain formation and dynamic recrystallization (Fig. 4c and d). Potassium feldspar shows dimensions of approximately 1 mm and sericitization to white mica. Plagioclase is abundant only in some samples and ranges in size between 0.2 and 1 mm in diameter with intense deformation and formation of irregular subgrains. It shows inclusions of biotite, zircon, and opaque minerals. The biotite lamellae are approximately 1–2 mm in thickness and occur scattered in the quartz-feldspar matrix parallel to the rock foliation (Fig. 4d). The mineralogic composition is quite similar to the rhyolitic member; however, the textures were modified because of the intense deformation related to regional shear zones.

The modal composition of the amphibolites is defined by anhedral to subhedral hornblende (75–90%), anhedral to subhedral plagioclase (20–30%), subhedral biotite (5%), anhedral chlorite, zircon (1%), opaque minerals (1%), and small amounts of anhedral quartz in a few samples (2–5%). The 0.5–1 mm-long hornblende crystals show irregular edges, altered to chlorite and biotite. Plagioclase grains are approximately 0.5–2 mm in length, deformed, and fractured. Biotite and chlorite are mainly secondary minerals. The rocks are strongly deformed, thus the original texture has been largely obliterated. Nevertheless, relict clinopyroxene, hornblende, and plagioclase minerals suggest an original basaltic composition.

In general, these rocks present a texture ranging from nematoblastic to nematogranoblastic and may show alternating mafic (hornblende and biotite) and felsic bands (plagioclase). The foliation is cut by late veins of secondary biotite resulting from alteration observed along the amphibole cleavages (Fig. 4e and f).

4. Analytical procedures

4.1. Whole-rock geochemistry

Eighteen representative samples of metavolcanic rocks (8 metarhyolites with rhyodacite and 10 amphibolites) from the NCGC were prepared for whole-rock geochemistry. The samples were crushed at the Geochronology Laboratory of the University of Brasilia and sent to the ALS Minerals Laboratory in Lima, Peru, for chemical analysis of major and trace elements, including rare earth elements. Major, trace, and rare earth elements were analyzed using inductively coupled plasma atomic emission spectroscopy (ICP-AES) with a detection limit of 0.01% and inductively coupled plasma mass spectrometer (ICP-MS) with a detection limit between 0.01 and 0.5 ppm after lithium metaborate/tetraborate fusion and digestion in nitric acid. The loss on ignition (LOI) was determined by the weight difference in the sample before and after heating at 1000 °C for approximately 1 h. Co, Cu, Li, Mo, Ni, Pb, Sc, and

Table 3
Zircon U-Pb of NCG 07 (amphibolite sample) from LA-ICP-MS.

Grain Spot	Isotope ratio						Age								
	$^{207}Pb/^{206}Pb$	± (1σ)	$^{207}Pb/^{235}U$	± (1σ)	$^{206}Pb/^{238}U$	± (1σ)	$^{207}Pb/^{206}Pb$	± (1σ)	$^{207}Pb/^{235}U$	± (1σ)	$^{206}Pb/^{238}U$	± (1σ)	Rho	Th/U	Conc. (%)
051-ZR28	0.12700	0.44	6.401	1.01	0.3655	0.83	2057	16	2032	18	2008	29	0.82	0.284	97.6
045-ZR23	0.13145	1.01	6.902	1.74	0.3808	1.36	2117	35	2099	31	2080	48	0.79	0.815	98.2
039-ZR19	0.13200	1.29	6.659	1.81	0.3659	1.22	2125	45	2067	32	2010	42	0.67	0.374	94.6
030-ZR14B	0,13100	1,58	6719	1,96	0,3719	1,10	2111	55	2075	34	2039	39	0,56	0,324	96,5
015-ZR5B	0,12659	0,38	6282	0,92	0,3599	0,75	2051	13	2016	16	1982	26	0,82	0,650	96,6
010-ZR5	0,12900	0,89	6505	1,43	0,3657	1,05	2084	31	2047	25	2009	36	0,74	0,041	96,4
028-ZR13B	0,12765	0,44	6996	0,97	0,3975	0,78	2066	16	2111	17	2157	29	0,81	0,463	104,4
041-ZR21	0,17661	1,27	10,392	3,14	0,4267	2,85	2621	42	2470	57	2291	110	0,91	0,080	87,4
040-ZR20	0,19170	0,63	12,752	1,06	0,4824	0,77	2757	21	2661	20	2538	32	0,73	0,151	92,1
020-ZR9B	0,19441	0,45	13,001	0,93	0,4850	0,72	2780	15	2680	17	2549	30	0,78	0,097	91,7
018-ZR8	0.18171	0.73	11.089	1.84	0.4426	1.65	2669	24	2531	34	2362	65	0.90	0.212	88.5
009-ZR4B	0.20172	0.78	14.608	1.99	0.5252	1.79	2840	25	2790	37	2721	79	0.90	0.080	95.8
007-ZR3	0.17788	0.38	10.814	0.85	0.4409	0.67	2633	13	2507	16	2355	26	0.78	0.163	89.4
016-ZR6	0.19396	0.43	13.188	1.03	0.4931	0.85	2776	14	2693	19	2584	36	0.83	0.167	93.1
052-ZR29	0.22490	0.47	16.124	1.22	0.5199	1.07	3016	15	2884	23	2699	47	0.87	0.125	89.5
031-ZR15	0.21806	0.86	14.182	2.58	0.4717	2.40	2966	28	2762	48	2491	99	0.93	0.298	84.0
027-ZR13N	0.21372	0.68	11.518	1.88	0.3908	1.71	2934	22	2566	35	2127	62	0.91	0.205	72.5
049-ZR27	0.27033	0.54	23.773	0.96	0.6378	0.71	3308	17	3259	19	3180	35	0.73	0.359	96.1
025-ZR11	0.26880	0.42	23.218	0.88	0.6264	0.68	3299	13	3236	17	3135	34	0.77	0.059	95.0
006-ZR2	0.26874	0.52	21.707	1.17	0.5858	0.98	3299	16	3171	23	2972	47	0.84	0.510	90.1
004-ZR1N	0.26026	0.54	20.386	1.25	0.5680	1.06	3248	17	3110	24	2900	50	0.85	2.127	89.3

Table 4
Zircon U-Pb of NCG10 (amphibolite sample) from LA-ICP-MS.

Grain Spot	Isotope ratio						Age								
	$^{207}Pb/^{206}Pb$	± (1σ)	$^{207}Pb/^{235}U$	± (1σ)	$^{206}Pb/^{238}U$	± (1σ)	$^{207}Pb/^{206}Pb$	± (1σ)	$^{207}Pb/^{235}U$	± (1σ)	$^{206}Pb/^{238}U$	± (1σ)	Rho	Th/U	Conc. (%)
004-ZR1	0.12618	0.43	6.247	1.01	0.3590	0.84	2045	15	2011	18	1978	28	0.83	0.371	96.7
035-ZR23	0.12292	0.52	5.762	1.19	0.3399	1.00	1999	18	1941	20	1886	33	0.84	0.142	94.4
029-ZR19	0.12696	0.72	6.430	1.24	0.3673	0.95	2056	25	2036	22	2017	33	0.76	0.496	98.1
040-ZR28	0.19610	1.14	14.073	1.55	0.5205	0.98	2794	37	2755	29	2701	43	0.64	0.942	96.7
036-ZR24	0.20200	0.47	14.602	0.93	0.5242	0.71	2842	15	2790	18	2717	31	0.76	0.218	95.6
026-ZR17N	0.19199	0.49	13.038	1.27	0.4925	1.11	2759	16	2682	24	2581	47	0.87	0.147	93.6
024-ZR15	0.18817	0.46	12.106	1.12	0.4666	0.95	2726	15	2613	21	2468	39	0.85	0.214	90.5
020-ZR14	0.18353	0.70	11.772	1.28	0.4652	1.00	2685	23	2586	24	2462	41	0.78	1.436	91.7
018-ZR12	0.18344	0.61	11.705	1.08	0.4627	0.81	2684	20	2581	20	2452	33	0.75	0.146	91.3
016-ZR10	0.19117	0.45	12.444	0.97	0.4721	0.78	2752	15	2639	18	2493	32	0.80	0.160	90.6
014-ZR9N	0.18480	0.48	11.644	1.07	0.4570	0.88	2696	16	2576	20	2426	36	0.82	0.144	90.0
013-ZR8	0.19690	0.57	13.577	1.20	0.5001	0.99	2801	18	2721	23	2614	43	0.83	0.144	93.3
008-ZR5	0.20103	0.91	14.909	1.52	0.5378	1.16	2835	30	2809	29	2774	52	0.76	0.992	97.9
039-ZR27	0.22632	0.93	14.548	1.39	0.4662	0.96	3026	30	2786	26	2467	39	0.69	0.075	81.5
019-ZR13	0.30977	1.37	28.903	2.05	0.6767	1.48	3520	42	3450	40	3332	77	0.72	0.366	94.7
028-ZR18	0.25642	0.62	19.095	1.45	0.5401	1.26	3225	20	3047	28	2784	57	0.87	0.485	86.3
025-ZR16	0.29215	0.47	25.983	1.02	0.6450	0.83	3429	15	3346	20	3209	42	0.81	0.394	93.6
010-ZR7	0.23424	1.13	15.310	1.47	0.4740	0.86	3081	36	2835	28	2501	36	0.58	0.147	81.2

Zn concentrations were obtained by multi-acid digestion and analyzed using ICP-AES with a detection limit between 1 and 10 ppm. Diagrams were created using the Geochemical Data Toolkit (GCDKIT) software and Excel sheets. The data are shown in Tables 1 and 2.

4.2. Zircon U-Pb geochronology

For U-Pb geochronological analysis of zircon grains at the Geochronology Laboratory of the University of Brasília, five samples were selected, two of amphibolite, one of metarhyolite, one of metarhyodacite, and one of hornblende-biotite paragneiss, for determination of the provenance of the detrital zircon. Isotopic analysis was conducted following backscatter electron (BSE) images that were used to investigate the internal structure of the zircon crystals prior to each analysis.

The samples were submitted for conventional preparation to separate zircon using crushing, gravimetric, and magnetic separation processes. Zircon grains were separated by density, using bromoform ($CHBr_{3-}$ relative density 2.89), and were handpicked using a binocular microscope. They were then mounted on epoxy resin for determination of isotopic ratios using a Thermo Finnigan Neptune multicollector ICP-MS equipped with a secondary electron multiplier-ion counter. For analyses of the sessions in the zircon grains the GJ-1 zircon provided by the ARC National Key Centre for Geochemical Evolution and Metallogeny of Continents (GEMOC, Jackson et al., 2004) and the 91500 zircon (Wiedenbeck et al., 1995, 2004) were used.

All data were reduced in Excel sheets following Bühn et al. (2009) and Chemale Jr. et al. (2012) and using the program Isoplot 4.15 (Ludwig, 2008). The results are shown in Table 3 through 7.

4.3. Nd-Sr isotopic composition

Sm-Nd and Rb-Sr analyses were performed on 26 samples at the Geochronology Laboratory of the University of Brasilia following the procedures described by Gioia and Pimentel (2000). Whole-rock powders (ca. 50–100 mg) were mixed with ^{149}Sm-^{150}Nd spike solution and dissolved in Savillex capsules. Sr, Sm, and Nd extraction of whole-rock samples followed conventional cation exchange techniques using Teflon

Table 5
Zircon U-Pb of sample NCG16 (Metarhyolite and metarhyodacites sample) from LA-ICP-MS.

Grain Spot	Isotope ratio						Age								
	$^{207}Pb/^{206}Pb$	± (1σ)	$^{207}Pb/^{235}U$	± (1σ)	$^{206}Pb/^{238}U$	± (1σ)	$^{207}Pb/^{206}Pb$	± (1σ)	$^{207}Pb/^{235}U$	± (1σ)	$^{206}Pb/^{238}U$	± (1σ)	Rho	Th/U	Conc.(%)
039-ZR26	0.12706	0.62	6.375	1.06	0.3638	0.78	2058	22	2029	19	2000	27	0.73	1.194	97.2
038-ZR25B	0.12760	0.54	6.138	1.34	0.3488	1.17	2065	19	1996	23	1929	39	0.87	0.904	93.4
033-ZR21	0.11661	0.74	4.265	1.90	0.2653	1.71	1905	26	1687	31	1517	46	0.90	0.334	79.6
030-ZR20	0.12735	0.61	6.502	1.04	0.3703	0.75	2062	22	2046	18	2031	26	0.72	1.075	98.5
029-ZR19	0.12736	0.57	6.313	1.07	0.3595	0.82	2062	20	2020	19	1980	28	0.77	1.164	96.0
028-ZR18	0.12740	0.50	6.689	0.99	0.3808	0.77	2062	17	2071	17	2080	27	0.78	1.283	100.8
026-ZR16	0.12275	0.54	5.023	1.58	0.2967	1.43	1997	19	1823	27	1675	42	0.91	0.786	83.9
025-ZR15	0.12504	0.40	5.901	0.94	0.3422	0.77	2029	14	1961	16	1897	25	0.81	0.244	93.5
024-ZR14B	0.12686	0.43	6.294	1.08	0.3598	0.92	2055	15	2018	19	1981	31	0.85	0.429	96.4
018-ZR12	0.12751	0.48	6.223	1.08	0.3539	0.89	2064	17	2008	19	1953	30	0.83	0.872	94.6
016-ZR10	0.12512	0.41	6.074	0.96	0.3521	0.78	2031	15	1987	17	1944	26	0.81	0.226	95.8
015-ZR9	0.12739	0.46	6.663	1.15	0.3793	0.99	2062	16	2068	20	2073	35	0.86	0.564	100.5
014-ZR8	0.12478	0.51	5.506	1.00	0.3200	0.78	2026	18	1901	17	1790	24	0.78	0.363	88.3
013-ZR7	0.12793	0.54	6.605	1.05	0.3744	0.83	2070	19	2060	19	2050	29	0.78	1.199	99.1
010-ZR6	0.12568	0.66	6.151	1.18	0.3550	0.91	2038	23	1998	21	1958	31	0.77	0.259	96.1
009-ZR5B	0.12091	0.60	4.853	1.37	0.2911	1.17	1970	21	1794	23	1647	34	0.86	0.222	83.6
007-ZR4	0.12718	0.40	6.226	0.99	0.3550	0.83	2059	14	2008	17	1959	28	0.84	0.922	95.1
006-ZR3	0.12602	0.37	6.017	0.86	0.3463	0.68	2043	13	1978	15	1917	22	0.79	0.336	93.8
005-ZR2	0.12699	0.37	6.310	0.84	0.3603	0.65	2057	13	2020	15	1984	22	0.78	0.789	96.5
004-ZR1	0.12597	0.40	6.033	1.04	0.3473	0.89	2042	14	1981	18	1922	30	0.85	0.817	94.1

Table 6
Zircon U-Pb of NCG28 (Metarhyolite and metarhyodacites sample) from LA-ICP-MS.

Grain Spot	Isotope ratio						Age								
	$^{207}Pb/^{206}Pb$	± (1σ)	$^{207}Pb/^{235}U$	± (1σ)	$^{206}Pb/^{238}U$	± (1σ)	$^{207}Pb/^{206}Pb$	± (1σ)	$^{207}Pb/^{235}U$	± (1σ)	$^{206}Pb/^{238}U$	± (1σ)	Rho	Th/U	Conc.(%)
038-ZR27	0.12686	0.53	6.474	1.04	0.3701	0.81	2055	19	2042	18	2030	28	0.78	0.913	98.8
037-ZR26	0.12660	0.46	6.210	1.01	0.3558	0.82	2051	16	2006	18	1962	28	0.81	0.318	95.6
034-ZR23	0.12808	0.52	6.536	1.09	0.3701	0.89	2072	18	2051	19	2030	31	0.81	0.991	98.0
033-ZR22	0.12832	0.56	6.724	1.23	0.3800	1.03	2075	20	2076	22	2077	36	0.84	1.162	100.1
030-ZR21	0.12728	0.88	6.671	1.45	0.3801	1.08	2061	31	2069	25	2077	38	0.75	1.155	100.8
029-ZR20	0.12647	0.64	6.500	1.18	0.3728	0.93	2049	22	2046	21	2042	32	0.78	0.330	99.7
028-ZR19	0.12636	0.55	6.221	1.03	0.3571	0.79	2048	19	2007	18	1968	27	0.76	0.668	96.1
027-ZR18	0.12658	0.48	6.172	1.03	0.3536	0.83	2051	17	2000	18	1952	28	0.81	0.574	95.2
026-ZR17	0.12492	0.45	6.062	0.92	0.3519	0.71	2028	16	1985	16	1944	24	0.78	0.361	95.9
024-ZR15	0.12647	0.52	6.244	1.22	0.3581	1.03	2049	18	2011	21	1973	35	0.85	0.571	96.3
020-ZR14	0.12689	0.74	6.617	1.33	0.3782	1.05	2055	26	2062	23	2068	37	0.78	0.313	100.6
019-ZR13	0.12624	0.66	6.359	1.34	0.3653	1.11	2046	23	2027	23	2007	38	0.82	0.631	98.1
018-ZR12	0.12720	0.60	6.362	1.29	0.3627	1.09	2060	21	2027	23	1995	37	0.84	0.320	96.9
016-ZR10	0.12366	0.45	5.244	1.42	0.3075	1.30	2010	16	1860	24	1729	39	0.91	0.268	86.0
015-ZR9B	0.12639	0.42	6.151	0.91	0.3529	0.72	2048	15	1998	16	1949	24	0.79	0.900	95.1
013-ZR8	0.12579	0.54	6.096	1.09	0.3515	0.88	2040	19	1990	19	1942	29	0.80	0.556	95.2
010-ZR7	0.12642	0.66	6.268	1.21	0.3596	0.95	2049	23	2014	21	1980	32	0.78	0.868	96.6
009-ZR6	0.12731	0.60	6.408	1.06	0.3650	0.80	2061	21	2033	19	2006	27	0.75	0.871	97.3
008-ZR5	0.12556	0.50	6.254	1.00	0.3612	0.78	2037	18	2012	17	1988	27	0.78	0.502	97.6
007-ZR4	0.12689	0.43	6.414	1.00	0.3666	0.83	2055	15	2034	18	2013	29	0.82	0.870	98.0
006-ZR3	0.12583	0.41	6.194	0.94	0.3570	0.77	2040	14	2004	16	1968	26	0.81	0.480	96.4
005-ZR2	0.12593	0.35	6.173	0.85	0.3555	0.69	2042	12	2001	15	1961	23	0.80	0.615	96.0
004-ZR1	0.12394	0.33	5.710	0.86	0.3341	0.71	2014	12	1933	15	1858	23	0.82	0.193	92.3

columns containing LN-Spec resin (HDEHP–diethylhexyl phosphoric acid supported on PTFE powder). Sr, Sm, and Nd samples were deposited on double Re filaments and isotopic measurements were performed using a Thermo Scientific Triton multi-collector mass spectrometer. Uncertainties in the $^{87}Sr/^{86}Sr$ ratio were better than ± 0.01(2σ) and for the Sm/Nd and $^{143}Nd/^{144}Nd$ ratios were approximately 0.4% (1σ) and ± 0.005% (1σ) respectively, based on repeated analyses of international rock patterns BHVO-1 and BCR-1. The $^{143}Nd/^{144}Nd$ ratio was normalized to $^{146}Nd/^{144}Nd$ at 0.7219 and the decay constant (λ) $6.54 \times 10^{-12} y^{-1}$ was used. $T_{(DM)}$ models were calculated using the DePaolo model (1988). The isotopic analyses of metavolcanic rocks are shown in Table 8.

5. Results

5.1. Whole-rock geochemistry of metavolcanic rocks

Whole-rock chemical analyses were performed for 10 representative amphibolite and 8 metarhyolite and metarhyodacite samples based on the selection of those that were the least altered. Because of the intermediate to high metamorphic grades and weathering, the analyzed rocks were classified using elements, which are considered less mobile.

Metarhyolites and metarhyodacites had high SiO_2 (73–76 wt%) and Al_2O_3 (13–15 wt%) contents, whereas the amphibolites had SiO_2 contents ranging between 50 and 57 wt%, MgO 5–6 wt.%, $Na_2O + K_2O$ 3 wt%, CaO 6–8 wt.%, Fe_2O_{3T} 11–13 wt%, TiO_2 near 1 wt%, and P_2O_5 0.04–0.1 wt%. In the diagram proposed by Pearce (1982), using high field strength (HFS) covariant elements such as Ti vs. Zr for basalts, the

Table 7
Detrital zircon U-Pb of NCG35 (hornblende-biotite paragneiss sample) from LA-ICP-MS.

Grain Spot	$^{232}Th/^{238}U$	$^{207}Pb/^{206}Pb$	1σ (%)	$^{207}Pb/^{235}U$	1σ (%)	$^{206}Pb/^{238}U$	1σ (%)	$^{207}Pb/^{206}Pb$	1σ (%)	$^{207}Pb/^{235}U$	1σ (%)	Conc. (%)
068-ZR50	0.117	0.26010	0.62	23.082	1.09	3203	41	3247	20	3230	21	98.6
067-ZR49	0.169	0.25346	0.53	21.052	0.97	3039	35	3207	17	3141	19	94.8
066-ZR48	0.287	0.20830	0.50	15.937	1.15	2845	44	2892	16	2873	22	98.4
065-ZR47	0.167	0.22034	0.91	15.738	1.26	2691	35	2983	29	2861	24	90.2
064-ZR46	0.200	0.12807	1.19	6.363	1.83	1984	46	2072	42	2027	32	95.8
060-ZR45	0.109	0.20364	1.16	14.747	1.84	2721	61	2856	38	2799	35	95.3
059-ZR44	0.489	0.12723	1.93	6.564	2.92	2049	76	2060	67	2055	51	99.5
058-ZR43	0.274	0.21045	0.65	15.625	1.09	2777	36	2909	21	2854	21	95.5
057-ZR42	0.303	0.20323	1.13	15.009	1.67	2765	52	2852	37	2816	32	96.9
056-ZR41	0.152	0.12845	1.14	6.320	1.74	1967	43	2077	40	2021	30	94.7
055-ZR40	0.104	0.15683	2.41	8.745	3.46	2189	91	2422	81	2312	62	90.4
053-ZR38	0.076	0.18188	0.63	11.797	0.98	2485	27	2670	21	2588	18	93.1
050-ZR37	0.038	0.21708	1.02	16.219	1.64	2791	55	2959	33	2890	31	94.3
049-ZR36	0.154	0.19833	0.77	13.603	1.27	2603	40	2813	25	2722	24	92.5
048-ZR35	0.173	0.26339	0.65	22.443	1.12	3102	41	3267	20	3203	22	94.9
047-ZR34	0.226	0.19087	0.50	12.480	0.86	2502	24	2750	16	2641	16	91.0
045-ZR32	0.116	0.18356	1.13	11.804	2.51	2468	90	2685	37	2589	47	91.9
044-ZR31	0.156	0.27347	0.62	23.835	1.09	3158	41	3326	19	3262	21	94.9
040-ZR30	0.002	0.20092	0.76	14.440	1.17	2704	35	2834	25	2779	22	95.4
038-ZR28	0.241	0.24088	0.93	19.477	1.54	2975	56	3126	30	3066	30	95.2
036-ZR26	0.278	0.27549	0.61	24.762	0.95	3235	31	3338	19	3299	18	96.9
035-ZR25	0.232	0.19548	0.67	13.738	1.05	2655	31	2789	22	2732	20	95.2
034-ZR24	0.209	0.24710	0.65	20.332	1.09	3017	38	3166	20	3107	21	95.3
030-ZR22	0.013	0.19464	0.87	13.410	1.22	2612	33	2782	28	2709	23	93.9
029-ZR21	0.289	0.24960	0.78	19.743	1.13	2923	34	3182	25	3079	22	91.8
027-ZR19	0.126	0.27681	0.44	25.412	0.84	3290	31	3345	14	3324	16	98.3
026-ZR18	0.221	0.19180	0.63	12.457	1.10	2488	34	2758	21	2640	21	90.2
024-ZR16	0.155	0.12603	1.69	6.017	2.37	1917	54	2043	59	1978	41	93.8
020-ZR15	0.007	0.21045	1.50	15.072	2.08	2697	61	2909	48	2820	39	92.7
018-ZR13	0.168	0.18451	0.52	11.780	0.98	2453	30	2694	17	2587	18	91.1
017-ZR12	0.155	0.20937	0.57	15.243	1.11	2733	39	2901	19	2831	21	94.2
016-ZR11	0.210	0.20557	0.85	14.610	1.32	2680	41	2871	28	2790	25	93.3
015-ZR10	0.214	0.26026	0.53	22.803	1.12	3171	46	3248	17	3219	22	97.6
014-ZR9	0.650	0.18467	0.81	12.344	1.53	2548	52	2695	27	2631	29	94.5
013-ZR8	0.348	0.21154	0.78	16.013	1.44	2821	52	2917	25	2878	27	96.7
010-ZR7	0.208	0.12497	1.70	6.148	2.51	1967	61	2028	60	1997	43	97.0
009-ZR6	0.165	0.20377	0.88	14.066	1.34	2616	40	2857	28	2754	25	91.6
008-ZR5	0.262	0.27930	1.70	26.842	3.76	3409	175	3359	53	3378	72	101.5
007-ZR4	0.118	0.22816	0.68	16.901	1.39	2772	52	3039	22	2929	26	91.2
006-ZR3	0.309	0.18120	0.55	11.850	1.09	2502	36	2664	18	2593	20	93.9
004-ZR1	0.156	0.13042	1.00	6.363	1.67	1953	43	2104	35	2027	29	92.8

amphibolites showed trends compatible with fractional crystallization in the development of a volcanic arc (Fig. 5a). On the K_2O vs. SiO_2 diagram after Peccerillo and Taylor (1976), the amphibolites and metarhyolite-rhyodacite plot between the calc-alkaline to tholeiite series (Fig. 5b). In the diagram of De La Roche et al. (1980), the felsic metavolcanic rocks show the composition of rhyolite, some varying to rhyodacite, whereas the amphibolites plot in the andesite-basalt and andesite fields (Fig. 5c). In the rock classification diagram using immobile elements of Winchester and Floyd (1977), the metavolcanic rocks show a geochemistry compatible with rhyolite-rhyodacite and basaltic magmas of subalkaline to andesitic composition (Fig. 5d), which is also reinforced by the Irvine and Baragar (1971) diagram (Fig. 5e).

In addition, on the Jensen (1976) diagram, the samples are also compatible with calc-alkaline magma series (Fig. 5f). These intermediate to acidic rocks may be the result of fractional crystallization product of basalts on the ocean floor as suggested by the trend in Fig. 5a. In the Zr-Ti/100-3*Y diagram (Pearce and Cann, 1973), the amphibolites plot between the calc-alkaline (CAB) and ocean floor (MORB) basalt fields (Fig. 5g). In another petrogenetic indicator after Wood (1980) using immobile elements such as Ta-Th-Hf/3, the amphibolites plot between volcanic arc and MORB, similar to that of the other diagrams (Fig. 5h). In the primitive mantle-normalized trace element spider diagram of McDonough and Sun (1995), the metarhyolite-rhyodacites show high fractionation, with high contents of large-ion lithophile elements (LILEs; Cs, Rb, Ba, Th and Sr) and negative anomalies of high field strength elements (HFSEs; Nb, Ta, P and Ti) recognized in arc magmas. Basaltic-andesite and andesite are characterized by positive Ba, Nb, La, and Zr peaks and negative Ta, P, Ti, U, Th, and Rb anomalies (Fig. 6a). In the primitive mantle-normalized rare earth element (REE) pattern from McDonough and Sun (1995), the basaltic-andesite and andesite show low light rare earth element (LREE) fractionation (La/Yb_N = 0.74–0.93) in relation to heavy rare earth element (HREE) (La/Sm_N = 1.84–2.31) and negative Eu anomalies (Eu/Eu* = 0.74–0.93). In contrast, the metarhyolites and-rhyodacites show strong LREE fractionation (La/Yb_N = 14.30–39.82) in relation to the HREE (La/Sm_N = 3.28–9.71) and negative Eu anomalies (Eu/Eu * = 0.47–1.02, Fig. 6b).

5.2. Zircon U-Pb geochronology

5.2.1. Basaltic-andesite and andesite

Sample NCG 07 represents a concordant lens exposed parallel to the regional foliation (see Fig. 3f). The zircon grains of this sample are slightly fractured and have dimensions of approximately 50–100 μm (Fig. 7a). Several grains have a prismatic shape with oscillatory zoning, Th/U ratios varying from 2.12 to 0.026, and a discrete overgrowth border. The analyzed grains are represented by a discordia (mainly due to Pb loss) line that points out to Mesoarchean ages (3051 ± 13, 2904 ± 37, and 2838 ± 22 Ma, Fig. 8a, b and c) interpreted as

Table 8
Nd and Sr isotopic data from metavolcanic-sedimentary rocks of Nicolau-Campo Grande Complex. Initial compositions recalculated to crystallization age (t).

Sample	Rock	Longitude	Latitude	Sm (ppm)	Nd (ppm)	$^{143}Nd/^{144}Nd$ (± 2SE)	$^{147}Sm/^{144}Nd$	εNd (today)	εNd (t)	Idade U-Pb (Ga)	T_{DM} (Ga)	$^{87}Sr/^{86}Sr$ (today)	$^{87}Sr/^{86}Sr$ (t)
NCG3	Amphibolite	−36°48′14.43″W	-9° 47′32.49″S	5.017	18.995	0.511675 ± 9	0.1597	−18.79	−9.1	2.054	–	0.71207	0.71019
NCG7	Amphibolite	−36°48′35.95″W	-9° 56′0.20″ S	3.780	12.993	0.511901 ± 16	0.1759	−14.37	−5.2	2.054	–	0.71165	0.71052
NCG10	Amphibolite	−36°46′56.02″W	-9° 54′54.65″S	3.888	12.129	0.512060 ± 10	0.1938	−11.27	−11.3	2.054	–	0.71093	0.70998
NCG11	Amphibolite	−36°44′5.65″W	-9° 47′29.51″S	3.994	12.377	0.512091 ± 14	0.1951	−10.68	−10.3	2.054	–	0.71108	0.71009
NCG12	Amphibolite	−36°49′16.08″W	-9° 52′24.37″S	3.918	12.217	0.512067 ± 20	0.1939	−11.14	−10,0	2.054	–	0.71225	0.71119
NCG32	Amphibolite	−36°48′16.53″W	-9° 54′10.17″S	9.145	37.366	0.511344 ± 16	0.1479	−25.24	−12.5	2.054	–	0.71135	0.71022
NCG33	Amphibolite	−36°39′52.55″W	-9° 37′36.16″S	9.832	38.977	0.511440 ± 25	0.1525	−23.37	−11.8	2.054	–	0.71137	0.71028
NCG34	Amphibolite	−36°48′47.49″W	-9° 59′10.51″S	10.64	40.782	0.511128 ± 42	0.1578	−29.46	−19.2	2.054	–	–	
NCG35	Amphibolite	−36°55′17.73″W	-9° 52′53.56″S	9.870	39.457	0.511364 ± 12	0.1512	−24.84	−13,0	2.054	–	–	
NCG36	Amphibolite	−36°51′45.65″W	−10°1′12.85″S	10.843	40.092	0.511466 ± 24	0.1635	−22.87	−14.1	2.054	–	–	
NCG37	Amphibolite	−36°49′10.05″W	−10°3′10.34″S	9.449	37.747	0.511341 ± 15	0.1513	−25.30	−13.4	2.054	–	–	
NCG38	Amphibolite	−36°48′44.01″W	−10°0′48.78″S	21.565	85.264	0.511364 ± 38	0.1529	−24.85	−13.3	2.054	–	–	
NCG17	Metarhyolite-rhyodacite	−36°51′20.89″W	-9° 49′45.73″S	2.488	15.892	0.510685 ± 16	0.0946	−38.10	−11.26	2.061	3.02	0.73321	0.72082
NCG18	Metarhyolite-rhyodacite	−36°55′19.08″W	-9° 46′18.64″S	2.489	15.837	0.510713 ± 30	0.0950	−37.55	−10.81	2.061	3.00	0.73406	0.71540
NCG19	Metarhyolite-rhyodacite	−36°48′3.86″W	-9° 45′22.26″S	2.499	16.043	0.510688 ± 14	0.0941	−38.05	−11.08	2.061	3.01	0.73331	0.72104
NCG20	Metarhyolite-rhyodacite	−36°51′20.40″W	-9° 39′14.18″S	2.796	18.585	0.510601 ± 17	0.0909	−39.73	−11.92	2.061	3.04	0.73331	0.72351
NCG21	Metarhyolite-rhyodacite	−36°46′5.31″W	-9°54′11.45″S	4.329	20.374	0.511581 ± 7	0.1284	−20.62	−2.66	2.061	2.61	0.73324	0.71396
NCG4	Hornblende-biotite paragneiss	−36°48′53.91″W	-9°46′14.07″S	6.294	25.621	0.511741 ± 20	0.1485	−17.49	−5.02	2.028	3.07	–	
NCG28	Hornblende-biotite paragneiss	−36°49′53.31″W	-9°44′32.58″S	4.405	20.836	0.511611 ± 24	0.1278	−20.04	−2.22	2.028	2.54	–	

inheritance. In addition, Pb loss during the Brasiliano/Pan-African tectono-thermal event is represented by lower intercept ages ranging in the broad interval between ca. 660 and 503 Ma (Fig. 8a, b and d). Sample NCG 10 was collected from one amphibolite exposure associated with hornblende-biotite paragneiss. The grains are slightly fractured, with dimensions of approximately 100 µm, Th/U ratios between 1.43 and 0.075, and some with irregular zonation and overgrowth (Fig. 7b). U-Pb analyses indicate crystallization ages of approximately 2054 ± 20 Ma (Fig. 8d) and Pb loss at ca. 636 Ma. In spite of the number of Mesoarchean ages of inherited zircon grains, 2054 ± 20 Ma (Rhyacian period) is interpreted as the crystallization age of the magmatic protolith (Fig. 8d).

5.2.2. Metarhyolite and metarhyodacites

Sample NCG16 represents a metarhyodacite lens related to low-angle tectonics in which the analyzed zircon grains are sub-rounded and show a homogeneous appearance and incipient oscillatory zonation. Similar U-Pb 2062-Ma ages were determined in the grain cores, indicating predominantly Rhyacian crustal sources for the parental magmas (Fig. 7c). The Th/U ratios between 1.28 and 1.07 attest to their igneous origin. The interpreted crystallization age of these samples is, respectively, 2061 ± 8.6 Ma and 2074 ± 7.6 Ma with a loss of Pb at 621 ± 43 and 527 ± 160 Ma (Fig. 9a and b).

Sample NCG28 corresponds to metarhyolite with zircon crystal shapes similar to sample NCG16 (Fig. 7c). They are homogeneous, discretely fractured, and have rounded edges resulting from abrasive corrosion. They show a peak at 2055 Ma (Fig. 7d) and a Th/U ratio between 1.15 and 1.16.

5.2.3. Detrital zircon U-Pb geochronology

Sample NCG35 of the hornblende-biotite paragneiss from the Nicolau-Campo Grande was collected for age determination, tectonic environment, and provenance.

Unfortunately, zircon grains in such rocks are rather scarce. However, the obtained data is in accordance with the metavolcanic age data. On the analyzed grains, BSE images indicated two grain populations s (Fig. 10):

I) Prismatic grains with visible concentric oscillatory zoning and a length between 50 and 400 µm;
II) Homogeneous grains without oscillatory zoning and an average length of approximately 100 µm.

Few fractures were observed in the grains and the Th/U ratios were between 0.65 and 0.002. The obtained ages were Paleoproterozoic to Archean with a maximum deposition age of approximately 2028 Ma (the youngest zircon, Fig. 10a). The most prominent peaks are of Archean age at 2779, 2850, 3066, and 3324 Ma (Fig. 10b). These peaks can represent a mixture between Archean and Proterozoic sources. Zircon morphology from both groups as well as the Th/U ratios indicate derivation from magmatic sources with recrystallization of inherited ancient cores.

5.2.4. Nd and Sr isotopic ratios

Nd-Sr analyses were performed on 19 samples from the Nicolau-Campo Grande metavolcanic-sedimentary sequence. Twelve amphibolite samples show $^{147}Sm/^{144}Nd$ ratios ranging from 0.14 to 0.19. These rocks show negative εNd values (εNd $_{(2.054Ma)}$ = −5.2 to −19.2) suggesting a significant contribution from a crustal component. Five samples of metarhyolite and metarhyodacite show lower $^{147}Sm/^{144}Nd$ ratios (0.09–0.12), $T_{(DM)}$ model ages between 2.61 and 3.04 Ga, and negative εNd values (εNd $_{(2.061Ma)}$ = −11.92 to −2.66). Two hornblende-biotite paragneisses samples show $T_{(DM)}$ model ages of 2.54 and 3.07 Ga and a εNd $_{(2028Ma)}$ deposition value between −2.22 and −5.02, confirming the provenance was a crustal component (Fig. 11).

$^{87}Sr/^{86}Sr$ $_{(2054Ma)}$ isotopic data in seven amphibolite samples show

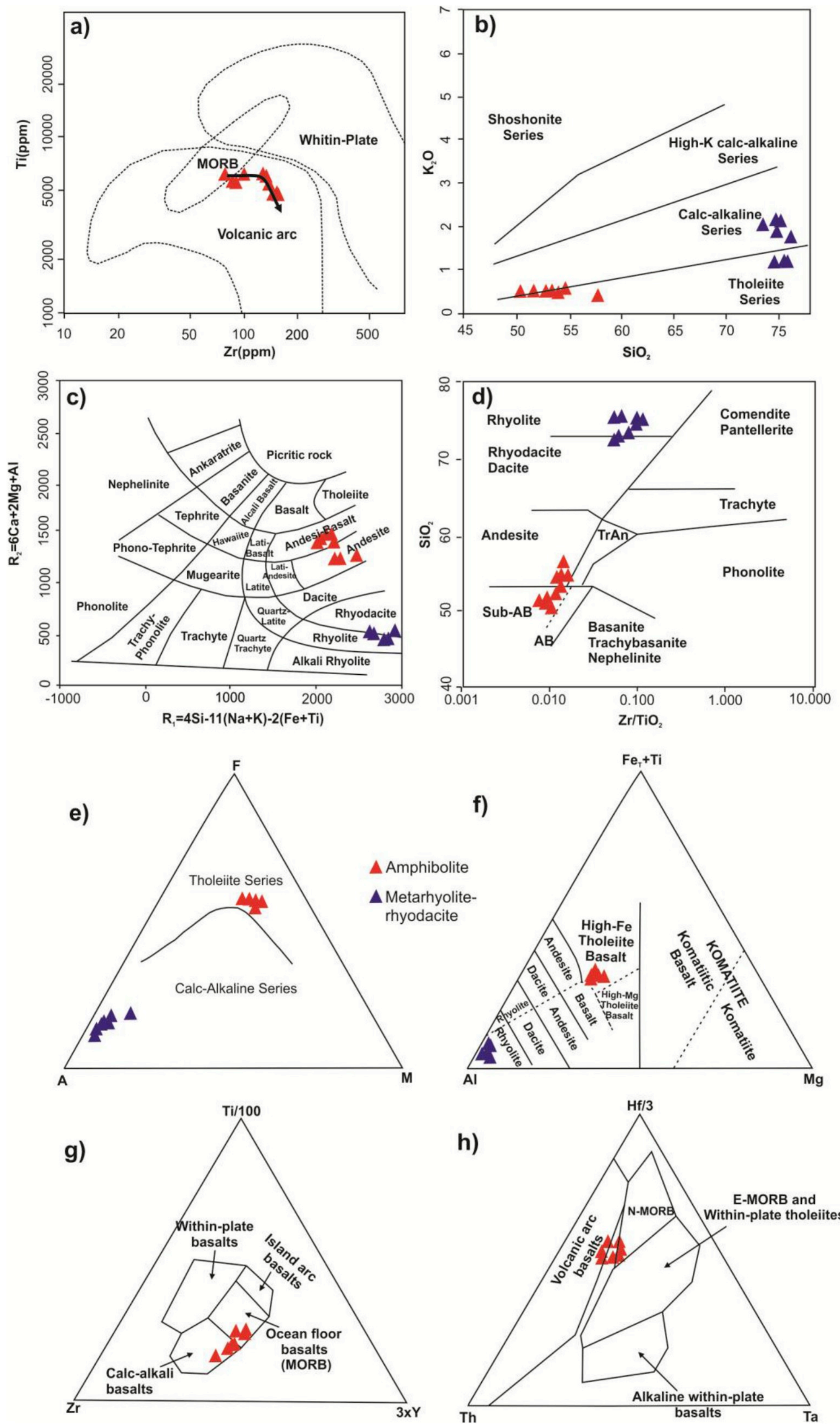

Fig. 5. Classification diagrams and tectonic environment for metavolcanic rocks a) Pearce (1982). b) Peccerillo e Taylor (1976). c) R_1-R_2 diagram of De La Roche et al. (1980) for cationic rate, where R1 = 4Si-11(Na + K)-2(Fe + Ti) and R2 = 6Ca + 2 Mg + Al. d) Winchester and Floyd (1977). e) Irvine and Baragar (1971). f) Jensen (1976). g) Pearce and Cann (1973). h) Wood (1980).

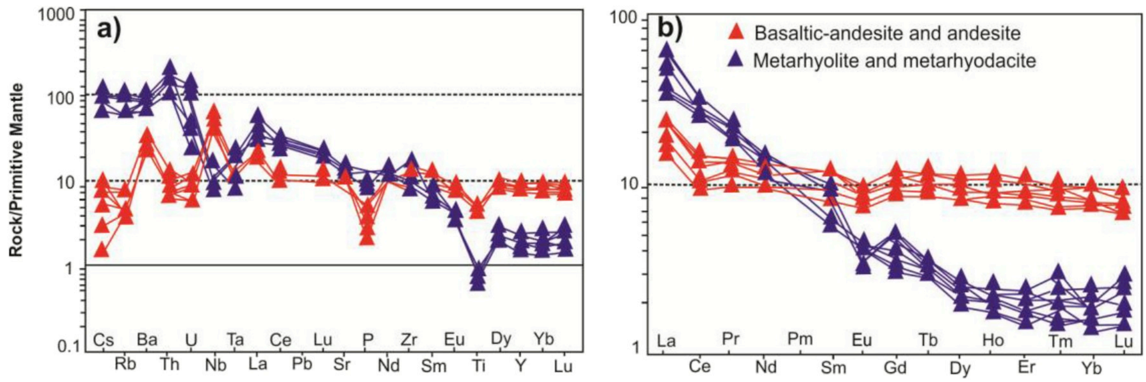

Fig. 6. a) Spider-diagram and b) REE diagram for metavolcanic rocks of Nicolau-Campo Grande Complex normalized to the primitive mantle (McDonough and Sun, 1995).

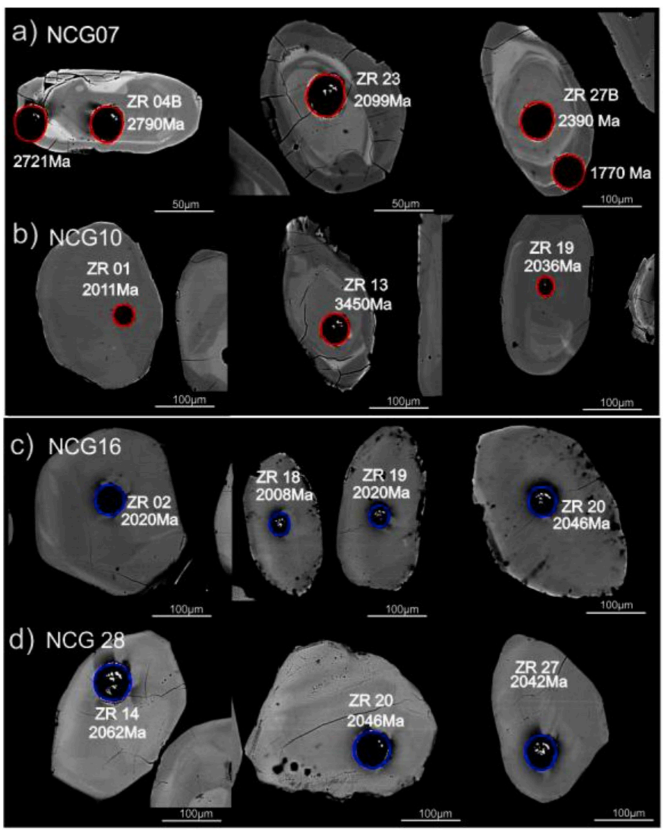

Fig. 7. BSE images of zircon grains from amphibolite, metarhyolite and metarhyodacites samples. a, b) NCG 07 and NCG 10 are zircon grains of amphibolites that were analyzed using laser spots with their respectively $^{207}Pb/^{206}Pb$ ages indicated by red circles. c,d) NCG 16 and NCG 28 are zircon grains of metarhyolites and metarhyodacites that were analyzed using laser spots and their respectively $^{207}Pb/^{206}Pb$ ages indicated by blue circles. (For interpretation of the references to colour in this figure legend, the reader is referred to the Web version of this article.)

initial values varying between 0.7099 and 0.7111 and five samples of metarhyolite and rhyodacites recalculated to crystallization age (2061 Ma) varied from 0.7139 to 0.7235 suggesting a strong crustal contribution for these rocks.

6. Discussion

The Sergipano Fold Belt represents an orogenic system consolidated in different phases of the Brasiliano/Pan-African orogeny and consists mainly of metasedimentary and metavolcanic rocks as well as granitic intrusions. (D'el Rey Silva, 1999; Oliveira et al., 2015). D'el Rey Silva (1999) was the first to interpret the Sergipano Fold Belt as the result of oblique collision between the São Francisco-Congo Craton and the Pernambuco-Alagoas Domain. In addition, in the belt, gneiss-migmatite basement domes are also recognized, known as the Jirau do Ponciano, Simão Dias, and Itabaiana domes.

In most Precambrian belts worldwide, plutonic domes have varied dimensions and arrangements and their origin is associated mainly with convergent tectonic environments and subsequent exposure via later extensional tectonics (Lee et al., 2000; Haris et al., 2002). They are generally exposed by structural windows in orogenic belts, presenting a high-grade metamorphic core, which is covered or surrounded by lower-grade metavolcanic-sedimentary rocks (greenschist to amphibolite facies; Whitney et al., 2004). In evolved collisional settings, such domes usually exhibit differentiated exhumation in relation to the host rocks (Teyssier and Whitney, 2002; Whitney et al., 2004; Yin, 2004). Moreover, older metamorphic domes are of unique importance, as they may represent deep roots of exhumed continental arcs, which are key elements for understanding crustal melting and crustal flow processes during the development of orogenic systems (Kruckenberg et al., 2011).

In this context, this contribution presents geochemical and isotopic data of the supracrustal rocks of the Nicolau do Campo Grande sequence, which is associated with the Jirau do Ponciano Dome. It includes metarhyolites, metarhyodacites, and amphibolites with metasedimentary rocks represented by paragneisses, schists, and quartzites (Fig. 2). The mafic metavolcanic rocks of the NCGC are represented by amphibolite lenses that are interleaved with biotite schists and paragneisses that are concordant with the regional foliation (Mendes et al., 2009; Brito and Mendes, 2011, Fig. 3f). The overall geochemical results presented in this study show that the amphibolites have a volcanic arc signature, which is compatible with the tholeiitic to calc-alkaline magmatic series and corresponds to a basaltic-andesite of intermediate composition (SiO_2 between 50 and 57 wt%). However, the studied metarhyolite-rhyodacites are acidic (SiO_2 > 65% wt.%) and show a typical calc-alkaline signature.

The fractionation in the multi-element spider diagram shows that the metarhyolite/metarhyodacites and amphibolites are poor in Ti, P, Ta, and Nb, indicating strong contamination from continental crust in an active continental margin setting (Wilson, 1989). In addition, the REE contents in the mafic and felsic metavolcanic rocks show a slight to moderate negative Eu anomaly, which is suggestive of a plagioclase-bearing source, also common in a continental magmatic arc environment (Wilson, 1989; Baier et al., 2008). Tectonic discrimination diagrams for amphibolites show oceanic floor affinities tending to calc-alkaline while the metarhyolite and rhyodacites have continental arc characteristics.

U-Pb zircon ages of the amphibolites (basaltic-andesite and andesite protoliths) indicate a Paleoproterozoic crystallization age of 2054 Ma

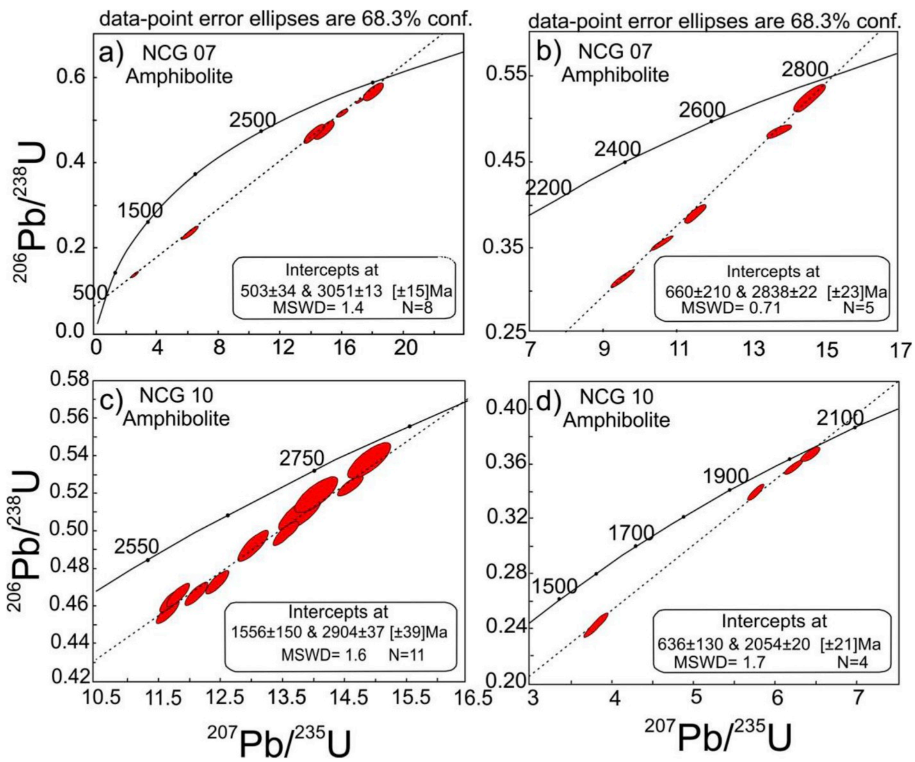

Fig. 8. Concordia diagram for LA-ICP-MS from amphibolite (basaltic-andesite) samples of Nicolau-Campo Grande Complex. Samples a,b) NCG 07 and c,d) NCG 10. The a,b and c) diagrams corresponded to Archean zircons intepreted as inherited cores while the d) diagram corresponded to Paleoproterozoic zircons (2054 Ma) intepreted as the best estimate for the crystallization age of the amphibolites.

(Rhyacian period) with a strong Mesoarchean inheritance (*i.e.* between 3051 and 2838 Ma), whereas the metarhyolites and metarhyodacites do not exhibit an Archean isotopic inheritance and clearly show Paleoproterozoic crystallization ages of approximately 2061 ± 8.6 and 2074 ± 7 Ma, respectively (Rhyacian period, Fig. 9a and b). In addition, detrital zircon grains from a hornblende-biotite paragneiss (sample NCG 35) show a wide range of ages, mostly Mesoarchean, and a Paleoproterozoic maximum deposition age (ca. 2027 Ma), which is in accordance with the obtained age for the metaplutonic members. For instance, previously obtained Rb-Sr data from Amorim et al. (1993) indicates the age of orthogneisses from the JPD at ~2.5 Ga, which can be attributed as the source of the detrital material of the NCGC paleobasin.

Furthermore, the Nd $T_{(DM)}$ model ages of the studied samples range from 2.54 to 3.07 Ga, indicating Archean crust participation in the evolution of the continental arc. Furthermore, these data are similar to the ages found in the migmatitic gneisses of the Simão Dias Dome (3.00–0.03 Ga) and biotite gneiss and granulite of the Itabaiana Dome (3.08–4.11 Ga) in the Vaza-Barris Domain and in rocks of the São Francisco Craton (2.13–3.54 Ga, Oliveira et al., 2015). According to these authors, the Itabaiana and Vaza Barris domes are likely sources for the original sediments of the Vaza Barris Domain. The average εNd values at 2054 Ma for the amphibolites between −5.2 and −19.2 suggest isotopic derivation from a preexisting felsic crust. The presence of the crustal component is attested to by the εNd at 2061 Ma in the metarhyolite and metarhyodacites between −11.92 and −2.66. In the two samples of hornblende-biotite paragneiss, the εNd at 2028 Ma was −2.22 and −5.02 representing a crustal source for the evolution of the Nicolau-Campo Grande paleobasin, which covered the plutonic Jirau do Ponciano Dome.

^{87}Rb-^{86}Sr isotopic data from previous studies of the orthogneiss of the Jirau do Ponciano Dome showed ages of approximately 2500 Ma (Amorim et al., 1993). However, the ^{87}Rb-^{86}Sr ratio is unstable in minerals as biotite and feldspar tend to be violated in open systems by thermodynamic events such as metamorphism, providing imprecise ages or incorrect initial ratios (White, 2015). ^{87}Sr/^{86}Sr $_{(2054Ma)}$ isotopic data for the mafic metavolcanic rocks of this complex show initial ratio values ranging from 0.7099 to 0.7111, which suggest crust reworking (Allègre, 2008; White, 2015).

Thus far, in the southern BP, recent obtained ages for gneissic-migmatitic rocks of the domes are Neoarchean (*e.g.,* 2729 Ma, Santiago et al., 2018), which is in accordance with previous published data from Oliveira et al. (2010) of ca. 2868 Ma. Such ages led these authors to interpret the gneissic domes of the Sergipano Fold Belt as part of the São Francisco Craton that were exposed by intense exhumation during the Neoproterozoic; however, we still do not have sufficient elements to interpret this for the Jirau do Ponciano Dome. In any case, it seems clear that continuous continental growth from the Archean to the Paleoproterozoic and subsequent erosion of the dome core led to the deposition of the supracrustal sequences of the NCGD, which were coeval to the arc-related volcanism.

Age correlatives with the studied rocks are widespread in the BP and West Africa. For instance, in the Pernambuco-Alagoas Domain to the north, Paleoproterozoic rocks occur within the Cabrobró Complex (2080–1570 Ma) and Archean zircons were identified in the Riacho Seco Sequence (2700 Ma, Cruz et al., 2015). In the central portion of the province, Paleoproterozoic events are responsible for reworking and eroding previous Archean crust in the Alto Moxotó Terrane, forming Paleoproterozoic calc-alkaline granites and supracrustal sequences Rhyacian in age (ca. 2.15–2.0 Ga, Santos et al., 2017). Such rocks record the strong inheritance of Archean zircon grains. Coeval sequences in Pan-African belts are also associated with continental arcs in the Eburnean orogenesis (ca. 2100 Ma). Reworking of Archean crust from gneissic-migmatitic domes and generation of Paleoproterozoic rocks in the Brasiliano Belts are also recorded in the Adamowa-Yaoundé Domain in the Central African orogenic belt, counterpart to the Sergipano Fold Belt (Tchakounté et al., 2017), as well as in the Nyong Group, Southwest Cameroon (Lerounge et al., 2006).

Therefore, based on the presented data, we suggest that the rocks of the NCGC are coeval to the development of the JPD. A proposed scenario suggest that this dome represents, at least in part, a remnant of a Paleoproterozoic-Archean continental arc root (TTG?), that was strongly exhumed by differential erosion. The deep remnants of this previous formed crust, was probably uplifted along thrust/backthrust

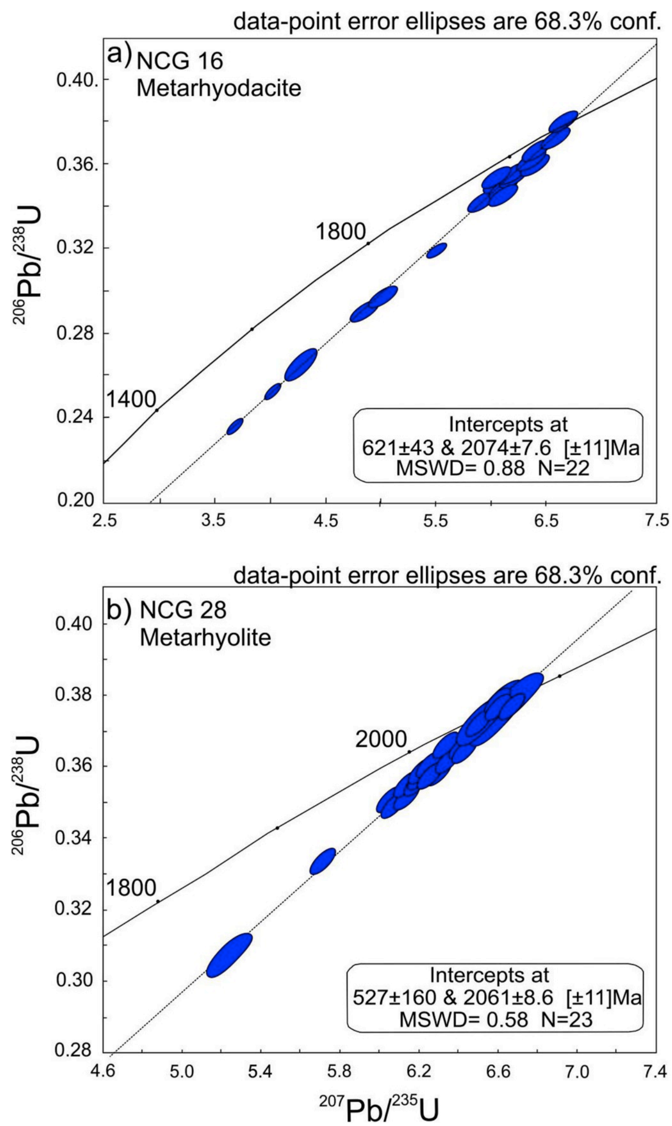

Fig. 9. Concordia diagram for LA-ICP-MS from metarhyolite and metarhyodacites samples of Nicolau-Campo Grande Complex. a) samples NCG16 and b) NCG28.

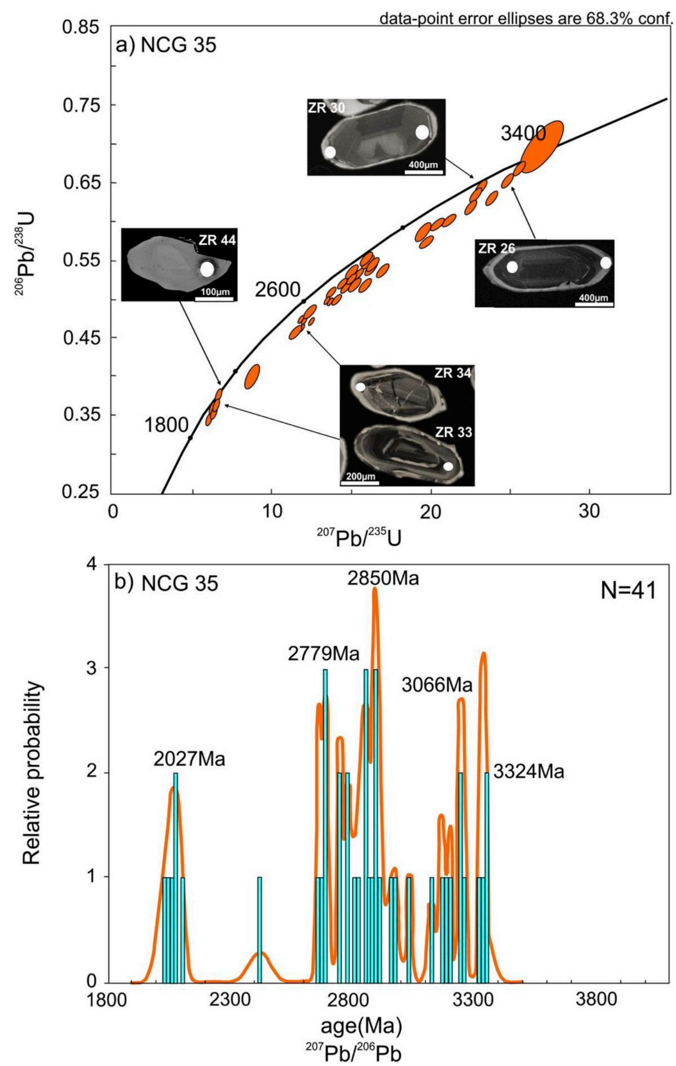

Fig. 10. a) Concordia diagram for detrital zircon grains from hornblende-biotite paragneiss NCG 35 and their respective images by BSE with laser spots indicated by white circle and b) Probability density plot.

faults, during the collision of the Pernambuco-Alagoas Domain and the São Francisco Craton, exposing part of the basement crust of the Sergipano Fold Belt.

7. Conclusions

Combining geological, whole-rock geochemical, isotopic, and geochronological data of the supracrustal rocks of the NCGC allowed for the following conclusions:

(a) The Nicolau-Campo Grande complex is spatially associated with gneisses and migmatites of the Jirau do Ponciano Dome. It is composed of metasedimentary rocks such as hornblende-biotite paragneiss, biotite-chlorite schist, metarhyolites, and amphibolites. Whole-rock major and trace-element geochemistry of the metavolcanic rocks indicate basaltic-andesite and rhyolitic to rhyodacitic protoliths with Ti, P, Ta, and Nb depletion, indicating the typical signature of a magmatic arc. Hence, chemical diagrams of the tectonic environment and petrotectonic association suggest a continental magmatic arc.

(b) Zircon U-Pb data of the metarhyolite and rhyodacites indicate Paleoproterozoic crystallization ages of approximately 2061 and 2074 Ma, respectively. However, zircon U-Pb data of the amphibolite samples show Paleoproterozoic ages (2054 Ma) and isotopic inheritance of Mesoarchean crust (2779–3324 Ma), whereas the U-Pb analysis of the detrital zircon grains from a hornblende-biotite paragneiss sample show a maximum deposition age of 2028 Ma and contributions from Archean sources. The Nd $T_{(DM)}$ model ages of the metarhyolite and metarhyodacites were 2.61 and 3.04 Ga and with continental derivation. The average εNd for the metavolcanic-sedimentary rocks showed a crustal component with a small contribution of mixing/interaction with a mantle component. The integration of isotopic data demonstrate the involvement of old crust, that can be attributed to the basement rocks of the Sergipano Fold Belt. It is the case of the Jirau do Ponciano Dome, which seems to represent a crustal TTG association, likewise others described in the Southern Borborema Province. The presence of Archean crust outlined by supracrustal sequences is a typical feature of Domic structures, exhumed and later exposed by structural windows in younger fold belts.

(c) The proposed tectonic scenario suggests the development of Paleoproterozoic magmatic arcs in the BP, thus, a part of the Gondwana basement. The results support Paleoproterozoic convergent tectonics, which can be attributed to accretionary processes

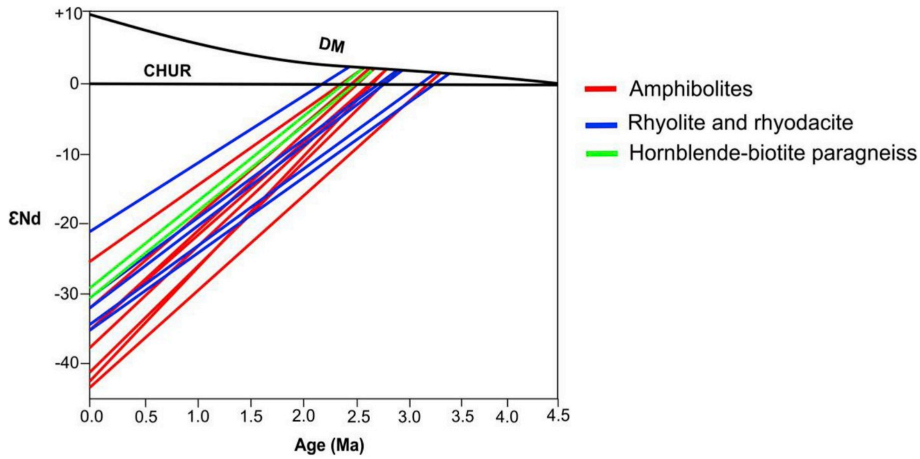

Fig. 11. Nd isotope evolution diagram for the metavolcanic and metasedimentary rocks of Nicolau-Campo Grande Complex.

between major continents such as Atlantica and/or minor microplates, leading to subsequent continental erosion and deposition of detritus related to the NCGC. Thus, we interpret that the metavolcanic-sedimentary sequence of the Jirau do Ponciano Dome is related to a magmatic arc root exhumed because of differential erosion that was later covered by the Neoproterozoic paleobasin that became the Macururé Domain in the northeast portion of the Sergipano Fold Belt.

Acknowledgments

This work was an integral part of the PhD project of the first author at the University of Brasília. The authors thank CNPq for financial support through grant 159762/2013-8 and the Geochronology Laboratory of the University of Brasília. We would like to express our gratitude to Editors James Kellog and Reinhardt Fuck as well as the anonymous reviewers for their valuable suggestions. Prof. Marcio Pimentel was the PhD advisor of the first author during the development of this research. He passed away just before this manuscript submission. This paper is kindly dedicated to his memory and legacy.

References

Allègre, C.J., 2008. Isotope Geology. Cambridge University Press.
Almeida, F.F.M., Hasui, Y., Brito Neves, B.B., Fuck, R.A., 1981. Brazilian structural provinces: an introduction. Earth Sci. Rev. 18, 1–29.
Amorim, J.L., 1995. Programa Levantamentos Geológicos Básicos do Brasil. Arapiraca, Folha SC.24-X-D-V. Estado de Alagoas. Escala 1:100.000, Brasília. CPRM, pp. 100.
Amorim, J.L., Torres, H.H.F., Silva Filho, M.A., 1993. O Complexo de embasamento da Faixa Sergipana na região de Jirau do Ponciano (AL): estratigrafia, evolução tectonometamórfica e potencialidade metalogenética. In: XV Simpósio de Geologia do Nordeste, Natal, pp. 240–242.
Baier, J., Audetat, A., Keppler, H., 2008. The origin of the negative niobium tantalum anomaly in subduction zone magmas. Earth Planet Sci. Lett. 267, 290–300.
Burg, J.P., Klaus, B.J.P., Podladchikov, Y.Y., 2004. Dome structures in collision orogens: mechanical investigations of the gravity/compression interplay. In: In: Whitney, D., Teyssier, C., Siddoway, S. (Eds.), Gneiss Domes in Orogeny 380. The Geological Society of America Special Paper, pp. 47–66.
Brito, M.F.L., Mendes, V.A., 2011. Compartimentação Tectônica da Folha Arapiraca. In: Simpósio Nacional de Estudos Tectônicos, Cuiabá, Mato Grosso, pp. 286–289.
Brito Neves, B.B., Fuck, R.A., Pimentel, M.M., 2014. The Brasiliano collage in South America: a review. Braz. J. Genet. 44, 493–518.
Brito Neves, B.B., Santos, E.J., Schmus, W.R.Q., 2000. Tectonic history of the Borborema province. In: Umberto Cordani; Edson José Milani; Antonio Thomaz Filho; Diogenes de Almeida Campos (Org.). Tectonic Evolution of South America. Rio de Janeiro: 31st International Geological Congress, pp. 151–182.
Brito Neves, B.B., Van Schmus, W.R., Santos, E.J., Campos Neto, M.C., Kozuch, M., 1995. O Evento Cariris Velhos na Província Borborema: integração de dados, implicações e perspectivas. Rev. Bras. Geociencias 25, 279–296.
Bühn, B.M., Pimentel, M.M., Matteini, M., Dantas, E.L., 2009. High spatial resolution analysis of Pb and U isotopes for geochronology by laser ablation multicollector inductively coupled plasma mass spectrometry (LA-MC-ICP-MS). An Acad. Bras Ciências 81, 1–16.
Chemale Jr., F., Kawashita, K., Dussin, I.A., Ávila, J.N., Justino, D., Bertotti, A.L., 2012. U-Pb zircon in situ dating with LA-MC-ICP-MS using a mixed detector conFigtion. An Acad. Bras Ciências 84, 275–295.
Cruz, R.F., Pimentel, M.M., Accioly, A.C.A., 2015. Provenance of metasedimentary rocks of the western Pernambuco-Alagoas domain: contribution to understand the Neoprote-rozoic tectonic evolution of the southern Borborema Province. J. S. Am. Earth Sci. 58, 82–99.
D'el-Rey Silva, L.J.H., 1999. Basin infilling in the southern-central part of the Sergipano Belt, NE Brazil, and implications for the tectonic evolution of the Pan-African/ Brasiliano cratons and Neoproterozoic sedimentary cover. J. S. Am. Earth Sci. 12, 453–470.
D'el-Rey Silva, L.J.H., McClay, K.R., 1995. The southern part of the Sergipano belt, NE Brazil: stratigraphy and tectonic implications. Rev. Bras. Geociencias 185–202.
De La Roche, H., Leterrier, J., Grandclaude, P., Marchal, M., 1980. A classification of volcanic and plutonic rocks using R1R2-diagram and major element analyses – its relationships with current nomenclature. Chem. Geol. 29, 183–210.
Depaolo, D.J., 1988. Neodimium Isotope Geochemistry-an Introduction. Springer-Verlag, pp. 490p.
Gióia, S.M.C.L., Pimentel, M.M., 2000. The Sm-Nd isotopic method in the geochronology laboratory of the University of Brasília. An Acad. Bras Ciências 72, 219–245.
Harris, L.B., Koyi, H.A., Fossen, H., 2002. Mechanisms for folding of high-grade rocks in extensional tectonic settings. Earth Sci. Rev. 9, 163–210.
Irvine, T.N., Baragar, W.R.A., 1971. A guide to the chemical classification of the common volcanic rocks. Can. J. Earth Sci. 8, 523–548.
Jackson, S.E., Pearson, N.J., Griffin, W.L., Belousova, E.A., 2004. The application of laser ablation inductively coupled plasma mass spectrometry to in situ U-Pb zircon geochronology. Chem. Geol. 211, 47–69.
Jensen, L.S., 1976. A new cátion plot for classifying subalkalic volcanic rocks. Ontario Div.Mines Misc 66.
Kruckenberg, S.C.O., Vanderhaeghe, E.C., Ferré, C., Teyssier Whitney, D.L., 2011. Flow of partially molten crust and the internal dynamics of a migmatite dome, Naxos, Greece. Tectonics 30, TC3001.
Lee, J., Dinklage, W.S., Hacker, B.R., Wang, Y., Gans, P.B., Calvert, A., Wan, J., Chen, W., Blythe, A., McClelland, W., 2000. Evolution of the Kangmar Dome, southern Tibet: structural, petrologic, and thermochronologic constraints. Tectonics 19, 872–896.
Lerouge, C., Cocherie, A., Toteu, S.F., Penaye, J., Milesi, J.P., Tchameni, R., Nsifa, N.E., Fanning, C.M., Deloule, E., 2006. SHRIMP U/Pb zircon age evidence for paleoproterozoic sedimentation and 2.05Ga syntectonic plutonism in the Nyong Group, Southwestern Cameroon: consequences for the eburnean-transamazonian belt of NE Brasil and central Africa. J. Afr. Earth Sci. 413–427.
Lima, H.M., Pimentel, M.M., Santos, L.C.M.L., Mendes, V.A., 2017. Análise tectônica da porção Nordeste da Faixa Sergipana, Província Borborema: dupla vergência em resposta a colisão obliqua entre o Cráton do São Francisco e o Terreno Pernambuco-Alagoas. Geonomos 25, 20–30.
Lima, H.M., Pimentel, M.M., Fuck, R.A., Santos, L.C.M.L., Dantas, E.L., 2018. Geochemical and detrital zircon geochronological investigation of the metavolcano-sedimentary araticum complex, Sergipano Fold belt: implications for the evolution of the Borborema province, NE Brazil. J. S. Am. Earth Sci. 86, 176–192.
Ludwig, K.R., 2008. User's Manual for Isoplot 3.70. A Geochronological Toolkit for Microsoft Excel. Berkeley Geochronology Center, Special Publication 4, pp. 75p.
McDonough, W.F., Sun, S.S., 1995. The composition of the Earth. Chem. Geol. 120, 223–253.
Mendes, V.A., Brito, M.F.L., Paiva, I.P., 2009. Programa Geologia do Brasil-PGB. Arapiraca. Folha SC.24-X-D. Estado de Alagoas, Pernambuco e Sergipe. In: Mapa Geológico. Escala: 1:250.000, Recife.
Neves, S.P., Bruguier, O., Silva, J.M.R., Mariano, G., Da Silva Filho, A.F., Teixeira, C.M.L., 2015. From extension to shortening: dating the onset of the Brasiliano Orogeny in eastern Borborema Province (NE Brazil). J. S. Am. Earth Sci. 58238–58256.
Oliveira, E.P., Mcnaughton, N., Windley, B.F., Carvalho, M.J., Nascimento, R. Silva, 2015. Detrital zircon U-Pb geochronology and whole-rock Nd-isotope constraints on sediment provenance in the Neoproterozoic Sergipano orogen, Brazil: from early passive margins to late foreland basins. Tectonophysics 662, 183–194.

Oliveira, E.P., Windley, B.F., Araújo, M.N.C., 2010. The Neoproterozoic Sergipano orogenic belt, NE Brazil: a complete plate tectonic cycle in western Gondwana. Precambrian Res. 181, 64–84.
Oliveira, E.P., Toteu, S.F., Araújo, M.J., Carvalho, M.J., Nascimento, R.S., Bueno, J.F., Mcnaughton, N., Basilici, G., 2006. Geologic correlation between the neoproterozoic Sergipano belt (NE Brazil) and the yaoundé belt (Cameroon, Africa). J. Afr. Earth Sci. 44, 470–478.
Peccerillo, A., Taylor, S.R., 1976. Geochemistry of eocene calc-alkaline volcanic rocks from the kastamonu area, northern Turkey. Contrib. Mineral. Petrol. 63–81.
Pearce, J.A., 1982. Trace elements characteristics of lavas from destructive plate boundaries. In: Thorpe, R.S. (Ed.), Andesites. John Wiley and Sons, London, pp. 525–548.
Pearce, J.A., Cann, J.R., 1973. Tectonic setting of basic volcanic rocks determined using trace element analyses. Earth Planet Sci. Lett. 19, 290–300.
Santiago, R.C., Leal, A.B., Marinho, M., Argollo, R., Barbosa, J., Rocha Júnior, E., 2018. Litogeoquímica e geocronologia dos ortognaisses migmatíticos do Domo de Itabaiana, Sergipe: uma suíte do tipo tonalito, trondhjemito e granodiorito? Geol. Usp. Série Científica 17, 81–98.
Santos, E.J., Van Schmus, W.R., Kozuch, M., Brito Neves, B.B., 2010. The Cariris Velhos tectonic event in northeast Brazil. J. S. Am. Earth Sci. 29, 61–76.
Santos, E.J., 1995. O Complexo granítico Lagoa das Pedras: acresção e colisão na região de Floresta (Pernambuco), Província Borborema. Instituto de Geociências, Universidade de São Paulo, São Paulo, Tese de Doutorado, pp. 219.
Santos, L.C.M.L., Dantas, E.L., Cawood, P.A., Santos, E.J., Fuck, R.A., 2017. Neoarchean crustal growth and Paleoproterozoic reworking in the Borborema Province, NE Brazil: insights from geochemical and isotopic data of TTG and metagranitic rocks of the Alto Moxotó Terrane. J. S. Am. Earth Sci. 79, 342–363.
Santos, L.C.M.L., Dantas, E.L., Cawood, P.A., Lages, G.A., Lima, H.M., Santos, E.J., 2018. Accretion Tectonics in Western Gondwana Deduced from Sm-nd Isotope Mapping of Terranes in the Borborema Province, NE Brazil 37. https://doi.org/10.1029/2018TC005130.
Santos, R.A., Martins, A.A.M., Neves, J.P., Leal, R.A., Org, 1998. Geologia e recursos minerais do Estado de Sergipe. Brasília, CPRM/CODISE, 157 p. 1 mapa, col. Escala 1:250.000. Programa Levantamentos Geológicos Básicos do Brasil – PLGB.
Teyssier, C., Whitney, D.L., 2002. Gneiss domes and orogeny. Geology 30, 1139–1142.
Tchakounté, J., Eglinger, A., Toteu, S.F., Zeh, A., Nkoumbou, C., 2017. The adamawa-yadé domain, a piece of archaean crust in the neoproterozoic central african orogenic belt (bafia area, Cameroon). Precambrian Res. 299, 210–229.
Van Schmus, W.R., Kozuch, M., Brito Neves, B.B., 2011. Precambrian history of the zona transversal of the Borborema province, NE Brazil: insights from Sm-Nd and U-Pb geochronology. J. S. Am. Earth Sci. 31, 227–252.
Van Schmus, W.R., Brito Neves, B.B., Hackspacher, P.C., Babinski, M., 1995. U/Pb and Sm/Nd geochronologic studies of the eastern Borborema Province, Northeast Brazil: initial conclusions. J. S. Am. Earth Sci. 8, 267–288.
Wiedenbeck, M., Hanchar, J.M., Peck, W.H., Sylvester, P., Valley, J., Whitehouse, M., Kronz, A., Morishita, Y., Nasdala, L., Fiebig, J., Franchi, I., Girard, J.P., Greenwood, R.C., Hinton, R., Kita, N., Mason, P.R.D., Norman, M., Ogasawara, M., Piccoli, P.M., Rhede, D., Satoh, H., Schulz-Dobrick, B., Skår, O., Spicuzza, M.J., Terada, K., Tindle, A., Togashi, S., Vennemann, T., Xie, Q., Zheng, Y.F., 2004. Further characterization of the 91500 zircon crystal. Geostand. Geoanal. Res. 28, 9–39.
Wiedenbeck, M., Allé, P., Corfu, F., Griffin, W.L., Meier, M., Oberli, F., Von Quadt, A., Roddick, J.C., Spiegel, W., 1995. Three natural zircon standards for U-Th-Pb, Lu-Hf, trace element and REE analyses. Geostand. Newsl. 19, 1–23.
Winchester, J.A., Floyd, P.A., 1977. Geochemical discrimination of different magma series and their differentiation products using immobile elements. Chem. Geol. 20, 325–343.
White, M.W., 2015. Isotope Geochemistry. Wiley-Blackwell, pp. 496p.
Whitney, D.L., Teyssier, C., Vanderhaeghe, O., 2004. Gneiss dome and crustal flow. In: Whitney, D., Teyssier, C., Siddoway, S. (Eds.), Gneiss Domes in Orogeny. The Geological Society of America, pp. 15–33 Special Paper 380.
Wilson, M., 1989. Igneous Petrogenesis. Chapman & Hall, pp. 466.
Wood, D.A., 1980. The application of a Th-Hf-Ta diagram to problems of tectonomagmatic classification and to establishing the nature of crustal contamination of basaltic lavas of the British Tertiary Volcanic Province. Earth Planet Sci. Lett. 50, 11–30.
Yin, A., 2004. Gneiss domes and gneiss dome systems. In: Whitney, D.L., Teyssier, C., Siddoway, C.S. (Eds.), Gneiss Dome and Orogeny Boulder, Colorado. Geological Society of America Special Punlication.